International Journal of Hydrogen Energy 205 (2026) 153183

Contents lists available at ScienceDirect

International Journal of Hydrogen Energy

journal homepage: www.elsevier.com/locate/he

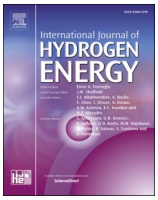

Activating aluminium for oxidation and hydrogen release: Overcoming the passivation barrier with superheated steam

N.W. Van de Velde [a,b], A. Drinčić [a], M. Grom [a], B. Likozar [a], B. Genorio [b], M. Haller [c], I. Jerman [a,*]

[a] National Institute of Chemistry, Ljubljana, 1001, Slovenia
[b] University of Ljubljana, Faculty of Chemistry and Chemical Technology, Ljubljana, 1000, Slovenia
[c] SPF Institute for Solar Technology, Eastern Switzerland University of Applied Sciences (OST), Rapperswil, 8640, Switzerland

ARTICLE INFO

Keywords:
Aluminium
Oxidation
Superheated steam
Hydrogen
Seasonal energy storage

ABSTRACT

Aluminium has considerable potential for use in seasonal energy storage, as it is energy dense and stable and can be recycled sustainably. However, a dense alumina barrier prevents energy extraction. In this work, aluminium is activated, and energy is extracted by oxidation using pressurized superheated steam. The activation of aluminium by penetrating the dense passivation layer requires the right feed material and reaction conditions. The onset mechanism is studied for low-yield reactions up to 2 %. In combination with pressures above 10 barG, microcracks form at temperatures above 500 °C. The diffusion of superheated steam through microcracks into the core of the aluminium results in oxidation past the passivation barrier and the evolution of H_2. This concept is further proven by the detection of Al_2O_3. This alternative reaction route in a dry oxidizing environment broadens the application range of aluminium as a metal fuel for long-term chemical energy storage.

1. Introduction

To address climate change and cope with geopolitical issues, fossil fuel restrictions and a transition towards more sustainable alternative energy sources are needed. Staying within reach of the Paris Agreement on Climate Change is possible by phasing out fossil fuels and focusing on improved energy efficiency. Energy can be harnessed from renewable sources, and many economic sectors can be electrified. To achieve the required electrification of the energy market, the capacity addition of renewables should triple in comparison to 2022 levels. An additional annual capacity of 1200 GW should be met by 2030, and more than 90 % of this expansion should be from renewables by 2027 [1,2]. Emission cuts in sectors that are difficult to electrify will be achieved by using low-emission fuels, sustainable bioenergy, and hydrogen-based fuels. In combination with society-driven changes and some carbon capture technologies, a modelled net zero CO_2 emission scenario by 2050 is targeted.

In the past 10 years, the levelized cost of electricity from solar and wind energy has gradually and globally become more competitive with that of fossil fuel-generated electricity. The market will therefore drive capacity expansion towards renewables, especially towards utility-scale solar energy additions. Variable renewables (VREs), such as solar and wind, are prone to short- and long-term fluctuations. Securing a stable energy supply requires a smart approach concerning VRE surpluses and deficits over different timescales and geographic areas. This smart approach involves the transformation between different types of energy and the availability of flexible energy storage over time. A surplus in energy when renewables are abundant will be used in times of deficit; this results in a more stable energy supply, better peak load management in the electrical grid and optimized cost per unit of energy. Energy storage systems (ESSs) based on different energy carriers—mechanical, chemical, electrochemical, electrical or thermal—are being extensively developed. All ESSs target specific application ranges and timescales. Fig. 1 gives a representation of several ESS techniques and energy carriers based on their energy storage capacities. Grid stability, energy management, power quality and short-term backup capacity are currently covered by superconducting magnetic energy storage (SMES) [3,4], capacitors [3,5], supercapacitors [3,6], flywheel energy storage (FES) [3,5] or batteries [3,7]. As the share of wind and solar energy in electricity production increases, periods of electricity surpluses or deficits will eventually increase as well. EES capacity must be developed to account for weekly, monthly and seasonal variations [8,9]. This

* Corresponding author. National Institute of Chemistry, Hajdrihova 19, Ljubljana, 1001, Slovenia.
E-mail address: ivan.jerman@ki.si (I. Jerman).

https://doi.org/10.1016/j.ijhydene.2025.153183
Received 21 August 2025; Received in revised form 11 November 2025; Accepted 21 December 2025
Available online 2 January 2026

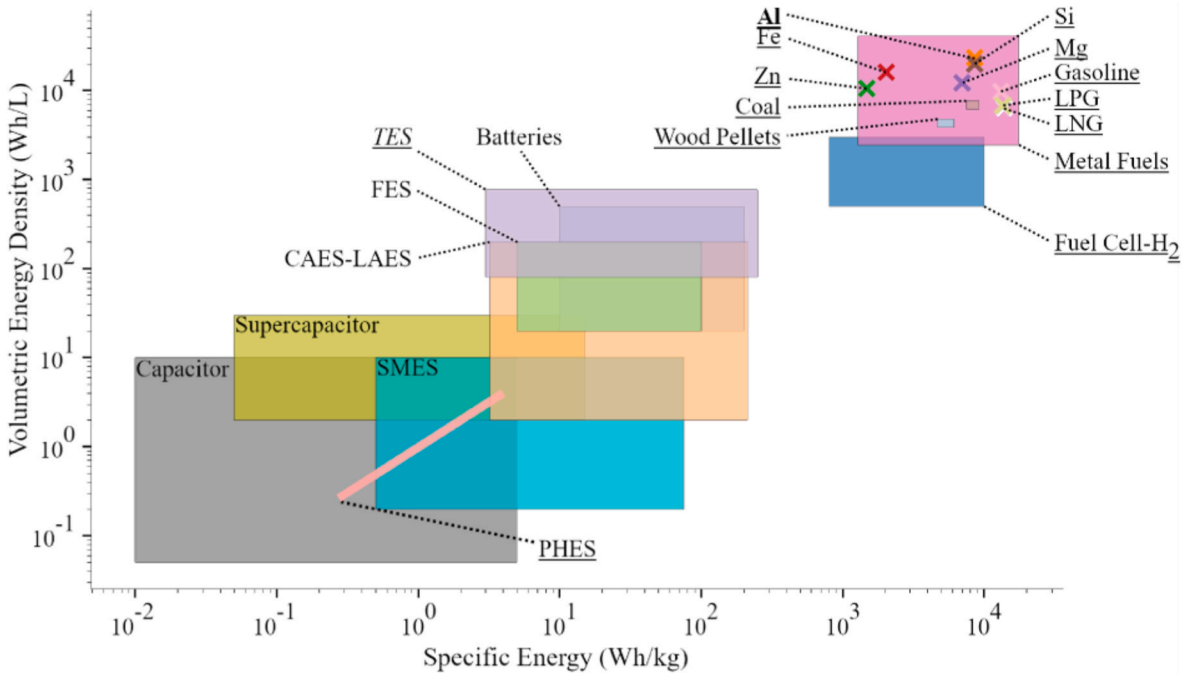

Fig. 1. Overview of energy storage systems, presenting their volumetric and weight-based energy density. Underlined ESSs have potential for long-term energy storage.

long-term energy storage requires appropriate characteristics in terms of energetic capacity, power capacity, storage time, and discharge time. Long-term variations are currently already governed by several ESS techniques or energy carriers, mainly by pumped hydro energy storage (PHES) [3,6], thermal energy storage (TES) [3,5], compressed or liquid air energy storage (CAES, LAES) [3,10] or by fossil fuel-based energy carriers [11] such as coal, gasoline, LNG or LPG. The first two have low energy densities, low flexibility and have environmental and geological limitations. The latter fossil fuel based alternatives do have high energetic density, but eventually need to be phased out. The development of green fuels with good stability and high volumetric and specific energy density is needed to add flexibility to the grid on a seasonal basis. In this way, the roll-out of additional renewable capacity remains economically and ecologically interesting. There is much interest in green H_2, which can be directly used in fuel cells or as a combustible fuel [3,5]. Biofuels, such as wood pellets [12], or e-fuels, which use H_2 indirectly, also serve as energy sources with appropriate characteristics for long-term energy storage. However, there are limitations. Direct use of H_2 requires the development of extensive H_2-related infrastructure, which suffers from compression and storage losses, and there are also safety restrictions. Additionaly, the indirect use of H_2 has the drawback of inherent efficiency losses related to multiple conversions (e.g., electricity to H_2, H_2 to green fuel, and green fuel to energy) [13]. Biofuels are limited by land and resource use and compete with crops for food consumption.

All of the abovementioned factors imply the need for an ESS with a long storage time, combining high energy capacity and volumetric energy density with convenient discharge times and long-term stability. Storing energy in a smartly chosen renewable and recyclable metal fuel (ReMeF) as a chemical energy carrier ("X") can deliver all these requirements. The long-term storage of the fuel is within reach if "X" has high specific energy, is chemically stable and is energy dense. In a Power-to-"X" cycle, excess renewable electricity is used to produce or recycle this energy carrier in a sustainable and circular way. Clean energy can thus be stored in metal fuels for use in times of deficit or transported to where energy is in high demand [14]. In this sense, aluminium is an interesting chemical energy carrier for long-term chemical storage [15,16]. Aluminium has an intrinsically high specific energy, good volumetric energy density, is highly abundant and can be sustainably recycled to close the material cycle. The latter is made possible by replacing graphite anodes in the Hall–Héroult smelting process with inert anodes [17]. All of these factors result in great potential for long-term energy storage, such as Power-to-X and energy supply, such as X-to-Energy - with "X" being aluminium. Domestic and off-grid energy supply becomes feasible when larger sized aluminium particulate matter is used as fuel. Using particulate matter >200 μm avoids logistical and safety issues during transport or handling. Therefore, aluminium is a promising energy carrier for resolving both seasonal and geographical supply and demand energy imbalances [18]. Alternative metal fuels with potential for sustainable energy storage are e.g., iron, magnesium, silicium and zinc [14,15].

The basic oxidation process of aluminium has previously been studied and is heavily restrained by the spontaneous formation of a thin (in the nanoscale range) passivation oxide layer in air. Al_2O_3 is created on the surface of the aluminium and protects the rest of the material from further oxidation under ambient conditions. This alumina layer is highly beneficial for long-term storage. However, activating the aluminium and breaking through this passivation layer beyond the nanoscale is essential for the overall energy conversion efficiency of the metal fuel. Ensuring that all possible energy from the exothermic oxidation reaction of aluminium can be extracted can be achieved in a few different ways. One activation option is direct combustion of small particles (in the μm range) in air using high flame temperatures to vaporize the protective oxide layer or melt the aluminium core [19]. Another activation method to bypass the passivation layer involves the penetration of the aluminium with low-melting-point eutectic mixes, e.g., with Ga [20,21]. Oxidation has also been proven to be possible in aqueous media. For fine particulate matter (in the nm–μm range), the passivation layer can be penetrated by water. This results in full oxidation and fast kinetics if the reaction temperature is 600 °C or higher [22. [23] Ultrasonic agitation can further improve the reactivity of fine aluminium powder [24]. Larger particulate aluminium matter (>200 μm) can be activated by disintegrating the passivation layer at low temperatures in basic media [25] or at high temperatures and pressures by working with supercritical steam [26,27]. High yields have been

demonstrated for the above oxidation in aqueous media, but challenges remain at the technological or safety level.

In the present work, we evaluate reaction conditions that allow hydrogen, oxygen or hydroxide ions to break through the protective oxide layer for larger granulate matter in a dry reaction medium under relatively moderate reaction conditions. The chosen granulate dimensions result in good handling and transport prospects. Heating saturated steam beyond its saturation temperature at a chosen reaction pressure results in very dry steam with high enthalpy and a better ability to penetrate the passivation oxide layer. Achieving oxidation under such conditions opens up the possibility to extract the stored energy for domestic, off-grid use. In addition to the chosen reaction conditions, the state of matter, dimensions, shape and composition of the raw material potentially influence the overall reactivity of the fuel in this approach. Chemical and morphological changes during the onset of the reaction were studied.

Releasing the energy chemically stored in aluminium occurs as follows.

1. Direct combustion in air [28].

$$4\ Al(s) + 3\ O_2(g) \rightarrow 2\ Al_2O_3(s)\ \Delta H_{r,298} = -1676\ kJ/mol$$

2. Oxidation in water – Low temperature [18].

$$2\ Al(s) + 6H_2O\ (l) \rightarrow 2\ Al(OH)_3(s) + 3H_2(g)\ \Delta H_{r,298} = -839\ kJ/mol$$

$$2\ Al(s) + 4H_2O(l) \rightarrow 2\ AlO(OH)(s) + 3H_2(g)\ \Delta H_{r,298} = -862\ kJ/mol$$

3. Oxidation in water–High-temperature/superheated steam [18].

$$2\ Al(s) + 3H_2O(g) \rightarrow Al_2O_3(s) + 3H_2(g)\ \Delta H_{r,298} = -950\ kJ/mol$$

Direct combustion of aluminium results in a theoretical energy release in the form of just heat (8.6 kWh/kg Al). However, the oxidation of aluminium in water generates both heat and H_2, where the energy stored in H_2 can be partially converted into electrical energy. This route leads to a thermal and electrical energy supply in convenient ratios for domestic energy consumption. For the studied high-temperature route (Eq. (3)), the exothermic reaction directly generates 4.9 kWh heat per kg of aluminium. Based on the chemical reaction, approximately 0.90 kWh will be used for the generation of steam, and 0.13 kWh will be used for heating 1 kg of aluminium to the reaction temperature. The energy stored in H_2 can be converted into a PEM fuel cell, with an electrical efficiency of up to 55 % and an additional recovery of 2/3 of the waste heat from the fuel cell in a combined heat and power setup [29]. Thus, H_2 results in up to 2.1 kWh of electrical energy and 1.1 kWh of thermal energy per kg of aluminium. In combination, the reaction of aluminium with superheated steam results in a highly exothermic reaction with a high specific energy of up to 8.1 kWh/kg. The in situ generation of H_2 and the complementary use of fuel cells for electricity generation are interesting, as they avoid safety issues in the transport and storage of H_2 for fuel cells. A benefit of this route is the formation of Al_2O_3 as a reaction product, which can be used directly as smelter-grade Al_2O_3 in the electrolysis cycle; this potentially avoids the additional energy consumed by calcination, e.g., $Al(OH)_3$ to Al_2O_3, when following the low-temperature oxidation route [30]. All available surplus renewable energy can thus be directly used in CO_2-free inert anode electrolysis from Al_2O_3 to Al-fuel. The round-trip efficiency is potentially increased, and the competitiveness with other EES or energy carriers increases. The presented dry route can additionally avoid the use of crystallization and sedimentation vessels in the reaction setup. In comparison to other chemical energy carriers or thermal energy storage, the main benefit of Alu-to-Power is its high volumetric energy density of aluminium. In comparison with, for example, borehole thermal energy storage (BTES), storage volumes can be up to 580 times lower. In comparison to compressed H_2 or liquid NH_3, the required storage volumes are up to 10 or 6 times lower, respectively, depending on the bulk density of the used aluminium fuel [31]. It has been shown that the levelized cost of energy storage is competitive with those alternatives, with the added benefit of lower transportation and operation costs [32]. The levelized cost of energy storage is currently approximately 180 €/MWh, which is lower than those of other common chemical energy carriers such as liquid H_2 (295 €/MWh), methane or methanol (265 €/MWh) or ammonia (310 €/MWh). Certain ESS techniques offer less expensive or comparable LCOES, such as TES (approximately 40 €/MWh) and H_2 storage in salt caverns (215 €/MWh) [8]. In addition to serving as a fuel for seasonal energy storage, the combined generation of heat and electricity is highly relevant for off-grid domestic energy supply. In mutual development with CO_2-free Power-to-Al energy storage techniques, this alternative approach to oxidize aluminium via superheated steam enables sustainable long-term energy storage with a high volumetric energy density of 22 kWh/L for pure aluminium. Combined with the existing and developing knowledge on recycling in Al smelter facilities, storing energy in aluminium offers a viable option to supply off-grid electricity and heat at competitive prices. The potential round-trip efficiency of aluminium fuel energy storage is approximately 45 %, which is comparable to those of other long-term ESSs. Liquid H_2 produced from fossil fuel reformation and stored for longer periods in large-scale hydrogen tanks has an energy efficiency of 45 %. Storing energy in methane (38–50 %), methanol (43–54 %) or ammonia (53 %) all have round-trip efficiencies comparable to that of storing energy in aluminium [8].

2. Materials and methods

2.1. Chemicals and materials

The oxidation reaction process was studied on aluminium fuel sources obtained from different providers. To evaluate the effects of material characteristics on the onset of the reaction, each material had a different chemical composition, shape or size.

A generic aluminium foil “GP15044SNEUT” was provided by AluFix (Vienna, Austria). “Aluminium (granulated) for synthesis” was purchased from Merck (Darmstadt, Germany) and served as larger particles with a low surface area. Medium-sized granulate matter is found in abrasive shot material. The spherical granulates used were “Aluminium shot granal” abrasive material from Eisenwerk Würth (Bad Friedrichshall, Germany), “Aluminium round” from Kuhmichel Abrasiv GmbH (Ratingen, Germany) and “Aluminium granules” provided by Metallpulver 24 (Sankt Augustin, Germany). Cylindrical shapes such as “Aluminium cut wire”, “Aluminium cut wire shot” and “Aluminium as cut” were obtained from Kuhmichel Abrasiv GmbH (Ratingen, Germany), KrampeHarex GmbH & Co. KG (Hamm, Germany) and Spajić (Negotin, Serbia), respectively.

2.2. Analytical techniques

Microscopy for particle size analysis and subsequent surface area estimation of the raw granular materials was performed using a 4× objective on a Bruker Hyperion 3000 microscope (Bruker, Billerica, Massachusetts, United States of America). Image processing for particle sizing was performed using ImageJ 1.54p software.

Surface analysis of aluminium before and after the reaction was performed using a Zygo Zegage 9000 Pro Hr optical profilometer (Zygo Corporation, Middlefield, CT, USA) and a WiTec Alpha 300 RA AFM (Witec, Ulm, Germany). Using optical profilometry, the surface morphology was scanned by a 50×0.55NA objective (FOV: 0.167 mm × 0.167 mm; optical resolution: 0.52 μm) using white LED light. The surface AFM scans were taken in amplitude-controlled tapping mode using reflex-coated cantilevers (42 N/m, 285 kHz) purchased from Witec. For both techniques, the results are presented after a 1st-order plane correction to partially offset the basic shape of the material and obtain a better representation of the surface details.

Table 1
Studied aluminium fuels.

Name in experiments	Name (Manufacturer)	Morphology	Production method	Manufacturer/Provider
Al-Foil	Alufix aluminium foil	Sheet	Hot and cold rolling	Alufix
Al–10Si	Aluminium shot granal	Granular - Spherical	Melt atomization	Eisenwerk Würth
Al-Deco	Aluminium granules	Granular - Spherical	Melt atomization	Metallpulver 24
Al-Rounded0.6	Aluminium round 0.6 mm	Granular - Spherical	Cut wire + conditioning	Kuhmichel Abrasiv GmbH
Al-Rounded0.8	Aluminium round 0.8 mm	Granular - Spherical	Cut wire + conditioning	Kuhmichel Abrasiv GmbH
Al-Rounded1.0	Aluminium round 1.0 mm	Granular - Spherical	Cut wire + conditioning	Kuhmichel Abrasiv GmbH
Al-Rounded1.2	Aluminium round 1.2 mm	Granular - Spherical	Cut wire + conditioning	Kuhmichel Abrasiv GmbH
Al-Merck	Aluminium (granulated) for synthesis	Granular - Cylindrical (Flattened)	N.A.	Millipore - Merck
Al-CutWire0.6	Aluminium cut wire 0.6 mm	Granular - Cylindrical	Cut wire	Kuhmichel Abrasiv GmbH
Al-CutWire0.8	Aluminium cut wire 0.8 mm	Granular - Cylindrical	Cut wire	Kuhmichel Abrasiv GmbH
Al-CutWire1.0	Aluminium cut wire 1.0 mm	Granular - Cylindrical	Cut wire	Kuhmichel Abrasiv GmbH
Al-CutWire1.2	Aluminium cut wire 1.2 mm	Granular - Cylindrical	Cut wire	Kuhmichel Abrasiv GmbH
Al-Krampe	Aluminium cut wire shot 1.0 mm	Granular - Cylindrical	Cut wire	KrampeHarex GmbH & Co. KG
Al-Spajic1.6	Aluminium as cut 1.6 mm	Granular - Cylindrical	Cut wire	Spajić

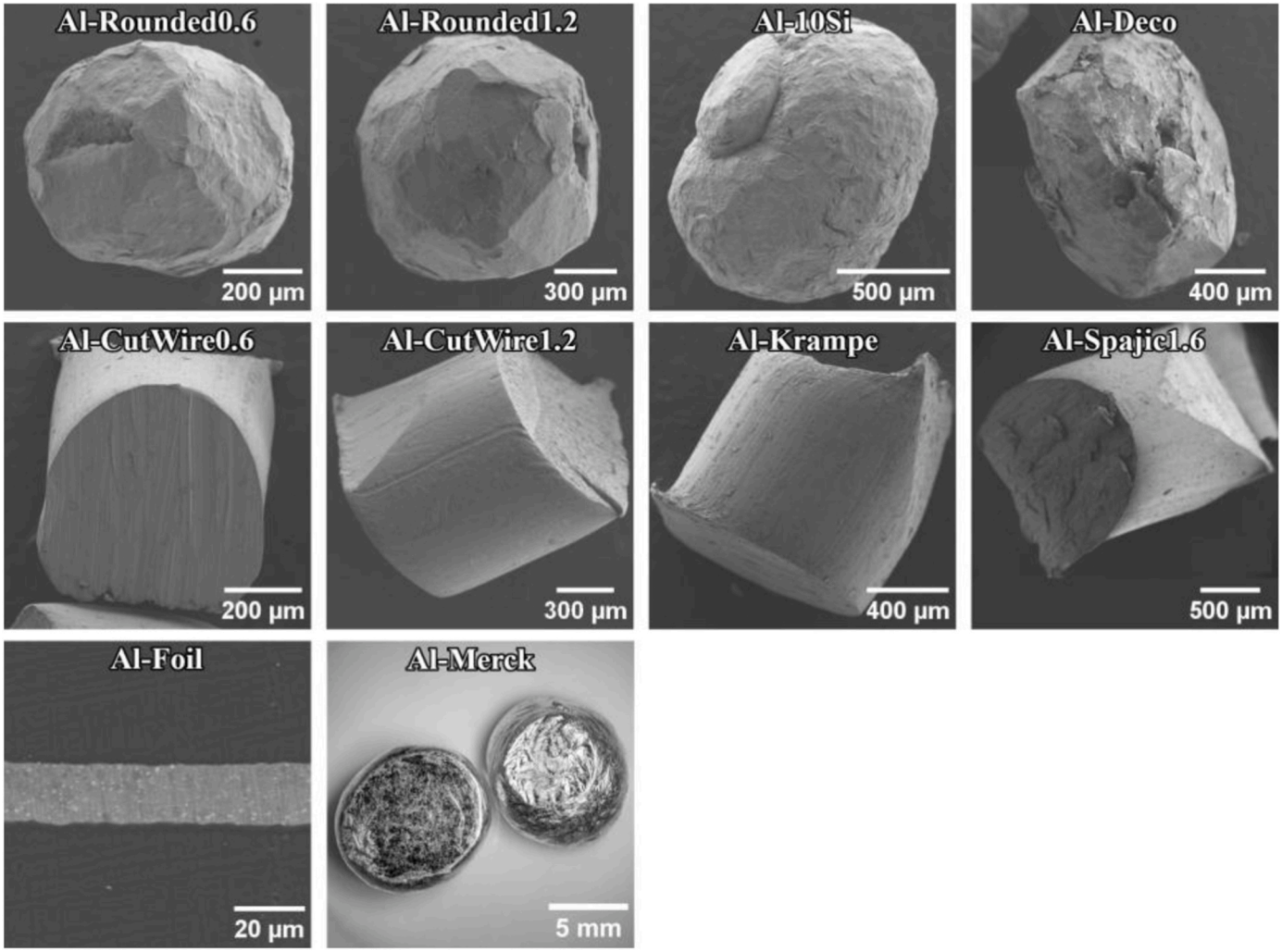

Fig. 2. Aluminium shape, size and morphology, imaged via SEM and optical microscopy (Al-Merck) Top row: Spherical granulate matter, Middle row: Cylindrical granulate matter, Bottom row: Other aluminium sources.

Surface and cross-sectional micrographs, together with local chemical analysis, were obtained on a Thermo Fisher Quanta 650 ESEM (Thermo Fischer, Waltham, Massachusetts, United States of America) with an EDS–AZtec Live with an Ultim Max SDD 40 mm^2 detector (Oxford Instruments, High Wycombe, United Kingdom) and on a Carl Zeiss Supra 35 VP HR-SEM (Zeiss, Oberkochen, Germany) with an EDS–AZtec Live with an Ultim Max SDD 100 mm^2 detector (Oxford Instruments, High Wycombe, United Kingdom). For the general surface morphology, an accelerating voltage of 2 kV was used for the incoming electron beam, whereas secondary electrons were collected with an ETD detector. The accelerating voltage of the incoming electron beam was 10 kV when the EDS signal was collected. The data resolution for EDS was 512 × 512 pixels for the measured mapping areas. Semiquantitative composition was obtained from mappings recorded in representative areas of at least 40 × 30 μm^2 (5.000× magnification). Cross sections of aluminium materials were prepared by immersion in epoxy and

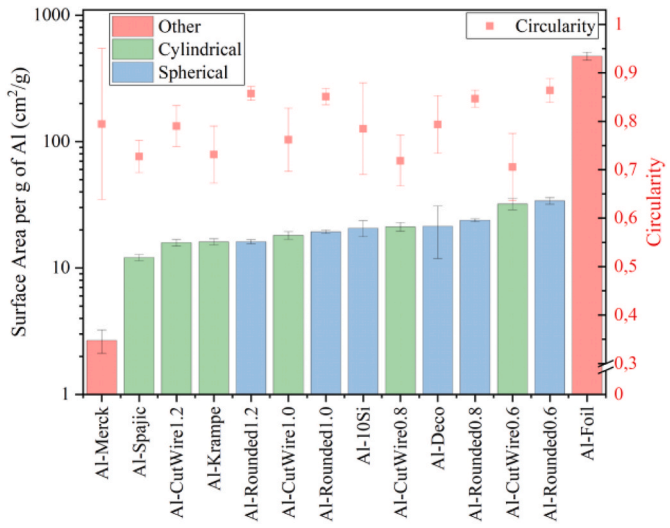

Fig. 3. Surface area per gram and circularity of aluminium based on particle size analysis for optical and electron microscopy images, with y-error bars showing the standard deviations for both parameters.

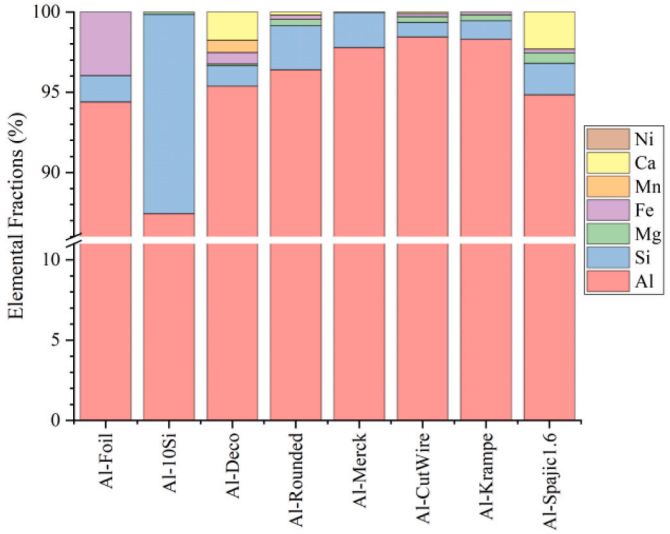

Fig. 4. Elemental composition based on cross-sectional EDS mapping analyses of different aluminium sources EDS analysis area magnification: 5.000×.

subsequent polishing. The polishing procedure involved a range of SiC sandpapers with decreasing roughness from P60 to P2500. Finally, a microcloth and 3 μm diamond suspension were added to create smooth cross sections, with sharp edges and minimal sample damage.

The sample density was determined via He pycnometry at 20 °C using a Micromeritics AccuPyc II 1345 pycnometer (Malvern Panalytical, Malvern, United Kingdom).

X-ray photoelectron spectroscopy (XPS) was performed with a Versaprobe 3 AD (Phi, Chanhassen, US) using a monochromatic Al-*Kα1* X-ray source. For each measurement, spectra were recorded using a 200 μm spot size (43.2 W, 45.0°). Survey spectra were measured using a pass energy of 224 eV and a step size of 0.8 eV. High-resolution (HR) spectra were recorded with a pass energy of 27 eV and a step size of 0.1 eV. To ensure high-quality spectral data with a good signal-to-noise ratio, at least 3 sweeps were performed for each measurement. The energy scale of the XPS spectra and any possible charging effects were corrected by referencing the C═C peak in the C 1s spectrum, with a binding energy (BE) of 284.8 eV. Argon ion (Ar^+) sputtering was used for depth profiling. The ion beam was operated at an accelerating voltage of 2 kV, and the spot size was 3 mm × 3 mm. Spectral processing was carried out using MultiPak 9.9.1 software, and Shirley background correction was applied to all the spectra. FT-IR chemical analysis of components present near the surface of the material was performed on a Bruker Vertex 70 V setup (Bruker, Billerica, Massachusetts, United States of America). Grazing incidence reflection FT-IR spectra were recorded for 64 scans under an incident angle of 80° using polarized light. The background was measured on a blank Au substrate.

3. Results and discussion

3.1. Aluminium

A selection of aluminium materials with 3 different geometric shapes, different particle sizes or different compositions was studied in the present work (see Table 1).

Aluminium materials were selected with safety and transport precautions in mind. The use of finer powders results in highly reactive materials under atmospheric reaction conditions due to their large active surface area. The related safety risks combined with their low bulk packing density between 0.05 and 0.25 g/cm^3 make them inconvenient for off-grid domestic energy supplies [33]. In that sense, a medium-sized granular material with particle sizes above 600 μm is a better compromise between surface area, safe handling and bulk packing density. These potential fuels are stable with respect to oxidation under atmospheric conditions. The bulk packing densities are between 0.9 and 1.7 g/cm^3 and have less effect on the theoretical volumetric energy density (d_{Al} = 2.7 g/cm^3). The shape of the granules is dependent on the production method and is generally either cylindrical for cut wire material or more rounded after additional mechanical treatment or after melt atomization from molten aluminium. Foil rolled aluminium is a third possible shape, which combines a high surface area with appropriate handling and transport properties. In addition, the bulk density of foil is potentially high.

The morphology and active surface area are two parameters that intuitively influence the interaction with superheated steam and are expected to influence the reactivity and final degree of conversion. The surface areas of the different materials were approximated based on their shape and dimensions, as observed via microscopy and SEM. Pore evaluation and density of the granulate matter were determined via helium pycnometry for Al-CutWire0.6 and Al-Rounded0.6. The respective densities were 2.691 and 2.696 g/cm^3, whereas the corresponding values were 2.70 g/cm^3 for the solid aluminium of the alloy type Al6060 [34]. This confirmed the very low porosity of the unreacted granulate material.

Based on the production method and SEM micrographs (Fig. 2), the studied materials were categorized by their geometrical shape (spherical, cylindrical, or other).

For all the granular materials, particle size analysis was performed in ImageJ software based on microscopy images taken of multiple granules. The 2D projected area and its distribution for multiple granules were obtained, together with parameters such as circularity and feret diameter. The surface area per granule was estimated based on the 2D projected area and its resulting equivalent diameter. Projecting the equivalent diameter onto perfectly spherical granules leads to an estimate of the surface area of the granules. When considering a density of 2.70 g/cm^3, the surface area per g of aluminium can be calculated for all the granules. For the foil material, thickness measurements were taken from cross-sectional electron micrographs and used to estimate the surface area. The active surface area is approximated by disregarding the surface roughness and porosity. The surface area of the granulated material ranged from 2.5 to 40 cm^2/g. Al-Foil has a substantially greater active surface area, at ± 500 cm^2/g (Fig. 3). The standard deviations of the surface areas of Al-Deco, Al-Merck and Al–10Si are greater than those of the other granules. The circularity values are highest for the rounded granules, with lower standard deviations and thus more regular

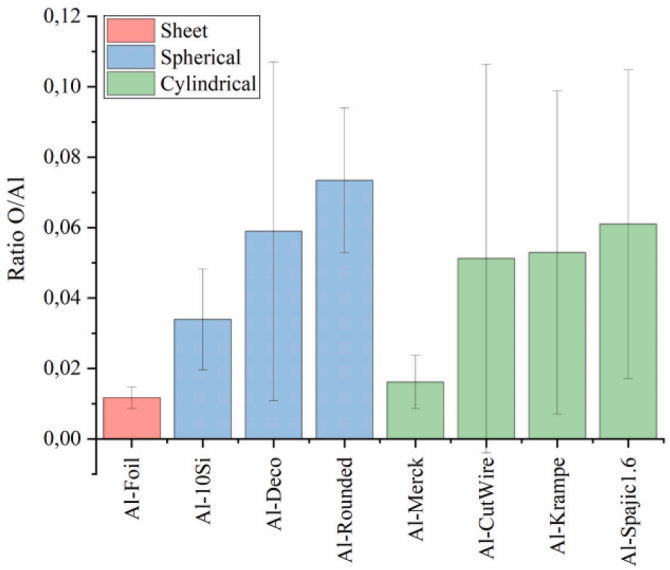

Fig. 5. O-to-Al ratios from EDS analysis performed on the surfaces of different untreated Al-fuels, with y-error bars for variations between measurement sites. EDS analysis area magnification: 5.000×.

shapes.

A third factor influencing the oxidation of aluminium is the chemical composition of the different materials. Various impurities can be present either by nature—originating from the raw materials in production—or as alloy elements to tune mechanical properties, corrosion resistance or handling characteristics. EDS analysis was performed for multiple representative areas of untreated materials after storage under ambient conditions. A semiquantitative compositional analysis of cross sections of aluminium in epoxy via SEM/EDS is presented in Fig. 4. The tested aluminium sources were classified as 3xxx (Al-Deco), 4xxx (Al-Merck, Al–10Si), 6xxxx (Al-CutWire, Al-Rounded, Al-Krampe, Al-Spajic) and 8xxx (Al-Foil) [35].

The growth of the passivation layer is thermodynamically governed and can be influenced by the composition of the alloy. In addition, the dissociation, chemisorption and diffusion of oxygen and the nucleation and growth of oxide materials can vary with composition [36]. Element maps taken on the surface of the raw materials revealed varying amounts of O and Al. Penetration of electrons and self-absorption of X-rays limit the range in which different elements can be detected. For lighter elements, the detection range is smaller than those for heavier elements, mainly due to high self-absorption for low-energy characteristic X-rays. The semiquantification of the amount of oxygen and aluminium on the surface is still related to the thickness and density of the oxide layer.

As shown in Fig. 5, the ratios between O and Al at the surface are low for aluminium foil, Al-Merck and Al–10Si, potentially indicating that it will be easier to overcome the oxidation barrier. The O-to-Al ratios are substantially higher and deviate more for the other granulates. Because Al-Merck has a low surface area and, as expected, low reactivity, aluminium foil and Al–10Si were selected to study the onset of the oxidation reaction at atmospheric pressure.

3.2. Reactor

An in-house-built laboratory-scale batch reactor with continuous steam production was used for the oxidation of aluminium. The reaction was monitored in situ by the evolution of H_2 gas. Changes in mass, morphology and chemical composition can subsequently be evaluated to gain insights into the reaction pathway; this allows assessment of the use of superheated steam to break through the protective passivation layer of larger particulate aluminium matter for different fuel materials.

A batch reactor with continuous superheated steam flux (Fig. 6) was built around a Bosio EUP-D 20/1200 muffle furnace (G) (Celje, Slovenia). Water flow and steam generation were controlled via a Flusys Wadose HP metering pump, where the ingoing water flow rate was set at

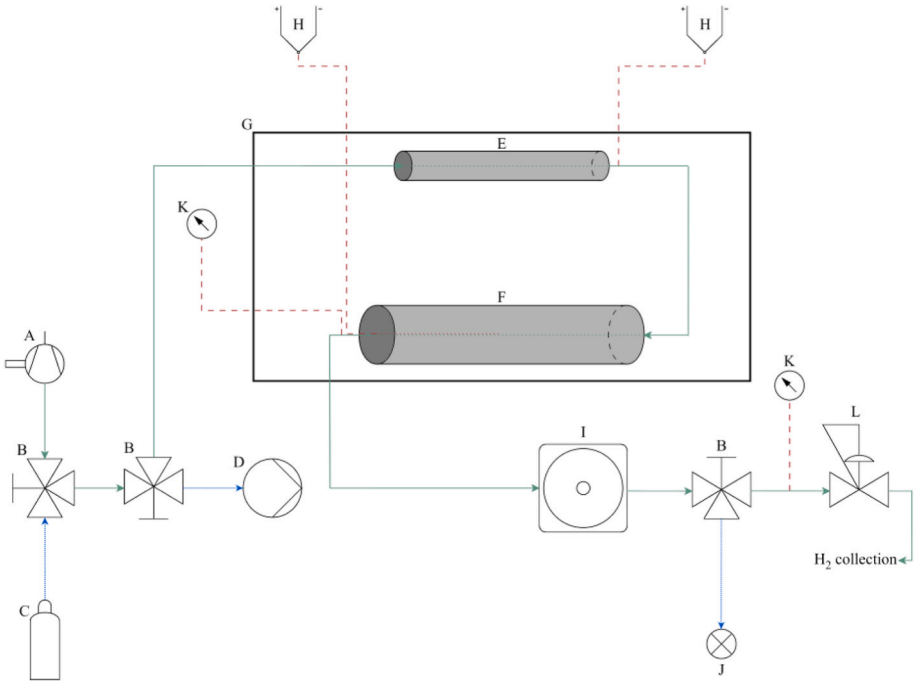

Fig. 6. P&ID diagram of the batch reactor: main (green)/auxiliary (blue)/monitoring (red) reaction lines. Components: (A) Vacuum pump, (B) 3-way valve, (C) N_2, (D) Wadose Flusys Metering Pump, (E) Steam boiler, (F) Aluminium reactor chamber, (G) Furnace, (H) Thermocouple reading, (I) Water cooling, (J) Exhaust point, (K) Pressure gauge, (L) Drastar backpressure regulator 1–50 bar. (For interpretation of the references to colour in this figure legend, the reader is referred to the Web version of this article.)

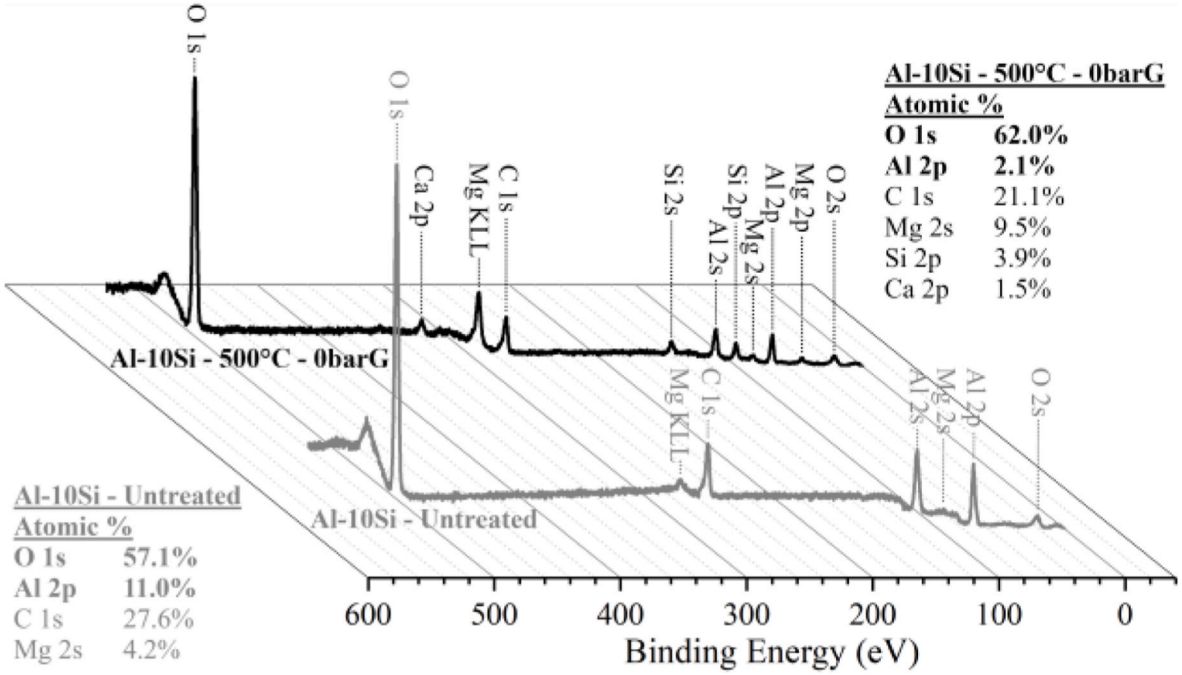

Fig. 7. XPS spectra and surface mapping of oxidized Al–10Si granules at 500 °C and atmospheric pressure for 6 h.

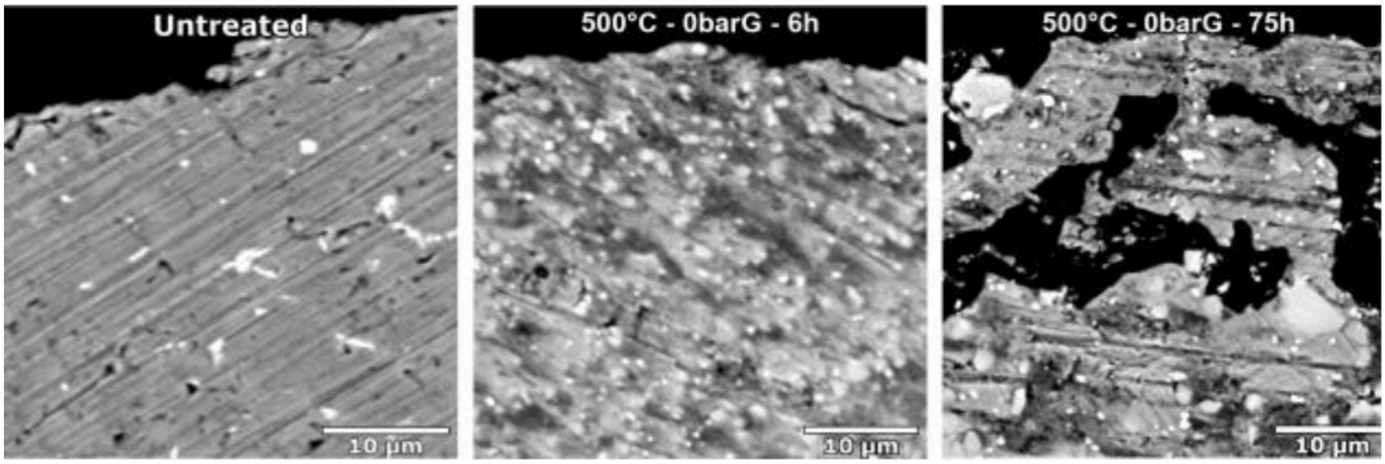

Fig. 8. Electron micrographs (BSE) of cross sections just below the surface of the Al–10Si granules before and after reacting at 500 °C and 0 barG for 6 h or 75 h (CBS detector; accelerating voltage: 10 kV). Magnification: 5.000×.

2.5 mL/min (D) (Offenbach am Main, Germany). Steam generation with temperatures above the critical temperature of water at the used reaction pressures was monitored by temperature readings after the steam boiler (H). The reaction pressure was controlled via a Drastar 088S-050A-1O–H1 (max 50 bar) (L) (Guro-gu, Seoul, South Korea) back-pressure regulator. Pressures were monitored with Ashcroft 68334-27 pressure gauges. The generated H_2 was collected behind a water lock. The connection tubes (1/16″), steam boiler (E) (15 cm, 1/2”), reaction chamber (length: 20 cm, internal diameter: 2 cm, reactor volume: 62.8 cm^3), and fittings and valves were stainless steel and were purchased from DK-Lok (Juchon-myeon, Gimhae-si, Gyeongsangnam-do, South Korea). The reaction conditions were limited to a temperature of 550 °C and a reactor pressure of 10 barG.

3.3. Onset of the oxidation reaction at atmospheric pressure

The onset of the oxidation reaction using superheated steam in a nonpressurized system was studied for 2 aluminium sources with low O/Al ratios, i.e., Al-Foil and Al–10Si.

With respect to Al–10Si, superheated steam-assisted oxidation at 500 °C and atmospheric pressure resulted in chemical and morphological changes near the surface that can be correlated with the oxidation of aluminium. XPS analysis of the aluminium before and after reacting for 6 h (Fig. 7) revealed relative differences in the atomic fractions of Al and O. The presence of oxygen near the surface of the untreated aluminium can be related to the presence of a passivation layer near the surface. The atomic ratio between oxygen and aluminium increases from 57/11 for the untreated sample to 62/2 for the oxidized sample. This observation shows that breaking through the passivation layer is possible through superheated steam-assisted oxidation. In addition to oxidation near the surface, XPS measurements also indicate that some alloying elements migrate towards the surface of the granules. The Si 2p and Ca 2p signals are detected only after the reaction, whereas the Mg 2s signal increases considerably after the reaction.

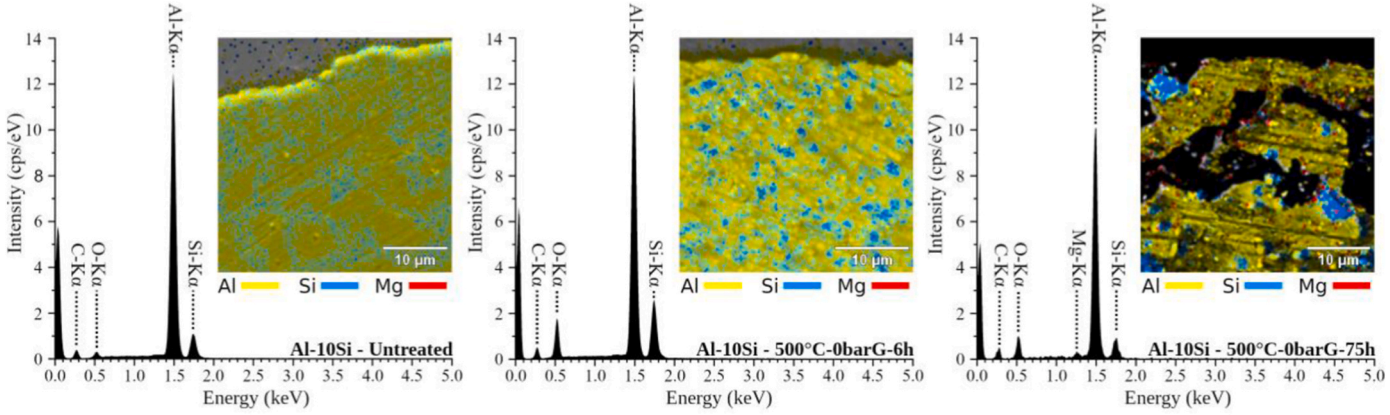

Fig. 9. EDS spectra and elemental mappings of cross sections of Al–10Si granules before and after superheated steam-assisted oxidation at 500 °C for 6 h or 75 h. EDS analysis area magnification: 5.000×.

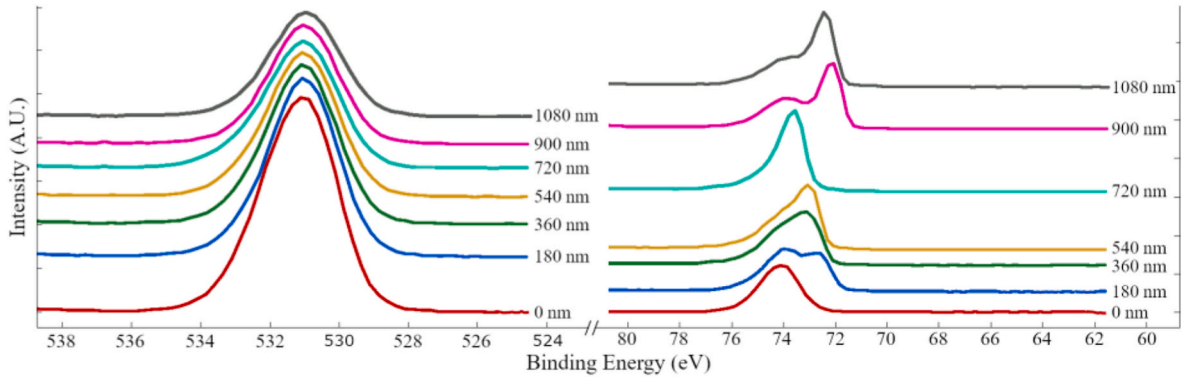

Fig. 10. XPS analysis of the Al-Foil samples (500 °C-0 bar/60 h). Depth profiles of the XPS signals for O 1s [left] and Al 2p electrons [right].

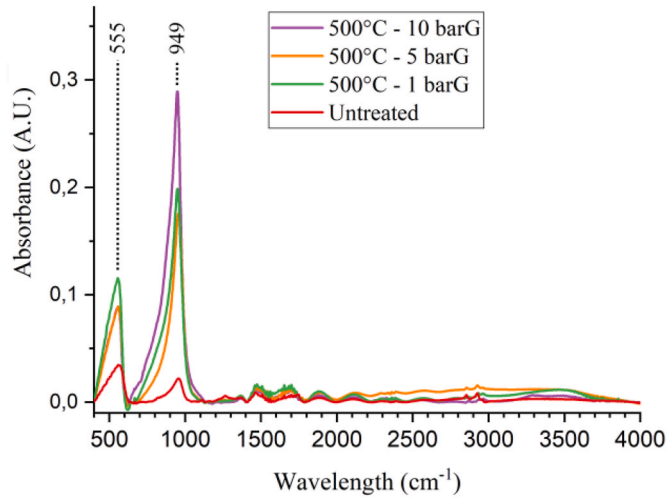

Fig. 11. Grazing incidence reflectance FT-IR spectra for Al-Foil before and after oxidation using superheated steam at 500 °C and pressures of 1, 5 and 10 barG for 6 h.

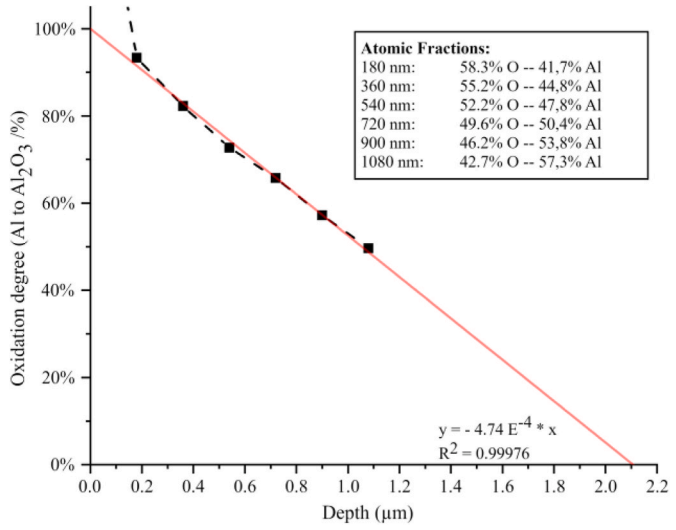

Fig. 12. Oxidation degree of Al-Foil (500 °C, 0 barG, 60 h) below the surface, as determined via XPS analysis.

Cross-sectional electron micrographs of the reacted Al–10Si samples show degradation of the material due to oxidation via superheated steam (Fig. 8). After oxidation at 500 °C for 75 h, the material visibly degraded to 25 µm below the surface of the granules. The particle diameter of Al–10Si is related to a maximum volume of 7 % that can be (partially) oxidized. Contact with the superheated steam for a shorter period of 6 h did not result in observable degradation below the surface of the material.

In addition to the breakdown of the material near the surface, the backscatter electron (BSE) images in Fig. 8 confirm the migration of the alloying elements. Brighter agglomerates accumulate near the surface of the granules after reacting with superheated steam for both 6 and 75 h

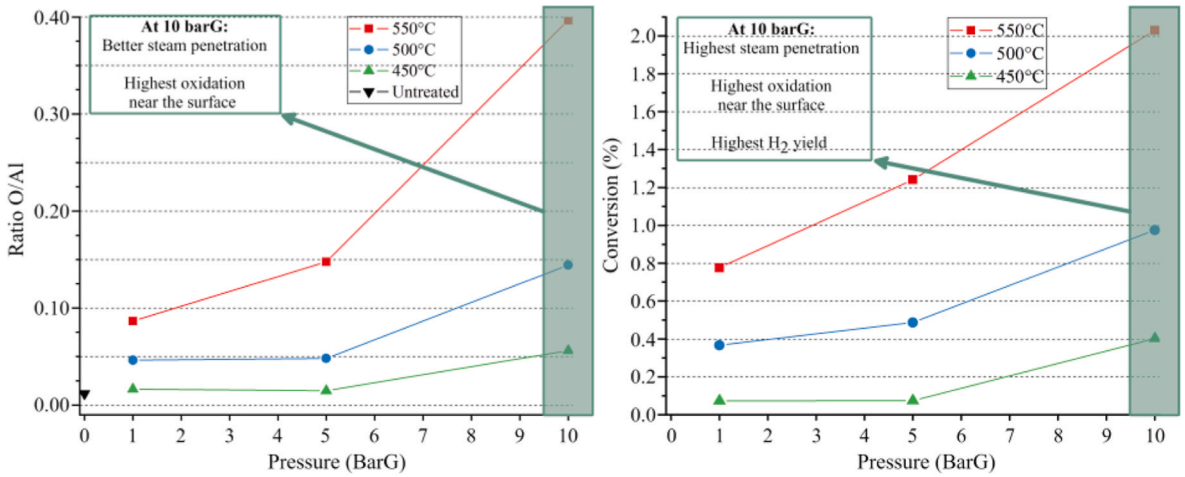

Fig. 13. Evaluation of Al-Foil oxidation using superheated steam at different temperatures (450, 500 and 550 °C) and pressures (1, 5 and 10 barG) for 6 h. Left: O-to-Al ratio from EDS analysis performed on the surface of the reacted foils. Right: Conversion degree based on H_2 yield after a 6 h reaction time. EDS analysis area magnification: 5.000×.

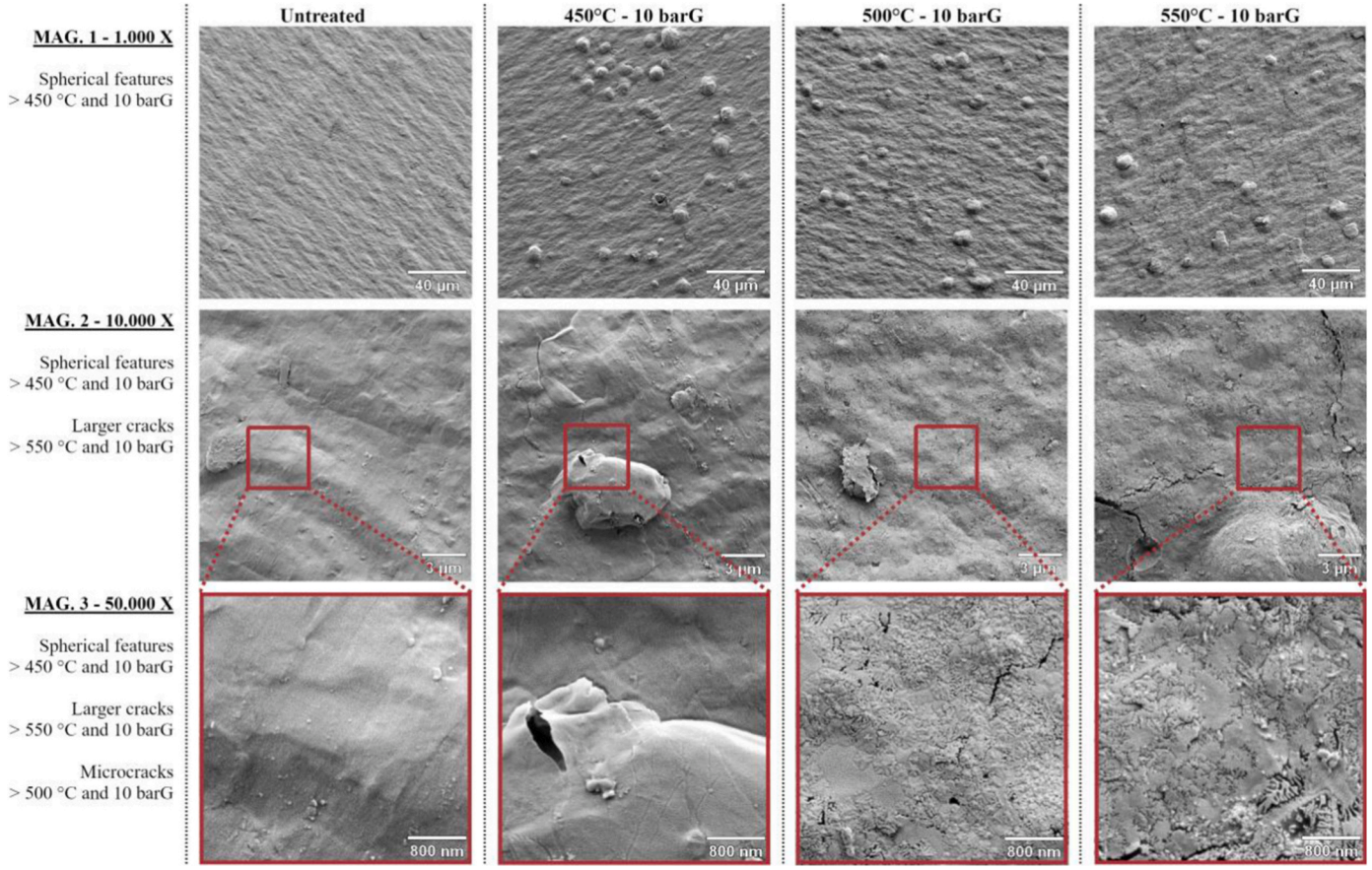

Fig. 14. SEM images of the Al-Foil surface after reaction at 10 barG (6 h) at reaction temperatures of 450, 500 and 550 °C and comparison with those of the untreated Al-Foil surface (ETD detector, accelerating voltage: 2 kV). Magnifications: Top row: 1.000×, Middle row: 10.000X, Bottom row: 50.000X

and become larger with increasing reaction time. Agglomerates of alloy elements near the surface are expected to influence the migration of atoms to the surface, causing mechanical disruptions in the oxide material and altering the subsequent oxidation reaction. The EDS mapping spectra in Fig. 9 show that these agglomerates are relatively rich in Si. The presence of Si can result in increased reactivity. Local embrittlement near the grain boundaries positively affects the interaction with superheated steam. However, the migration of Si can also result in decreased grain boundary energy. This can negatively impact any diffusion-related processes [20]. EDS mapping spectra taken closer to the surface, in the more degraded top part of the granule after 75 h of reaction, revealed an increasing amount of Mg. The presence of Mg as an alloy element could affect oxidation through a different mechanism. At high temperatures, diffusion towards the surface eventually leads to the formation of a secondary MgO phase. Differences in thermal expansion coefficients between MgO and Al_2O_3 can mechanically crack the passivation layer

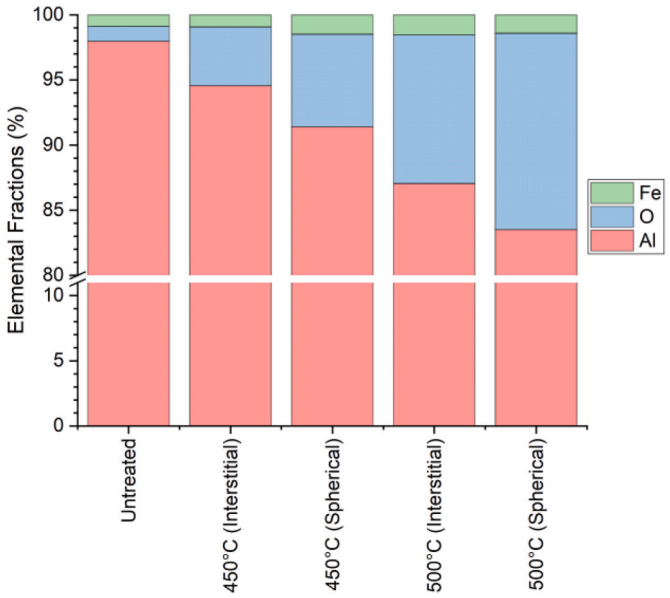

Fig. 15. Elemental quantification via surface EDS mapping, showing the chemical composition of features observed via SEM after 6 h of oxidation at 10 barG and temperatures of 450 and 500 °C. EDS analysis area magnification: 5.000×.

[37]. The experiments presented in Fig. 9 reveal that the diffusion behaviour is different for different alloying elements. Mg seems to diffuse towards the surface of the granules but does not form visible agglomerates, whereas Si does form large agglomerates. BSE images and EDS spectra confirm the observations made via XPS.

Chemical and morphological changes near the surface indicate that superheated steam can break through the passivation layer of the granules at ambient pressure. Degradation deeper into the material under atmospheric conditions seems to be limited to the upper shell of the granules, even for extended reaction times. The limited reaction kinetics and low overall yield of the oxidation do not result in observable H_2 generation; this might be improved by the use of aluminium sources with larger active areas.

Al foil is promising for further study of the oxidation process, as it combines a low O/Al ratio near the surface of the raw material (Fig. 5) with a high surface area (Fig. 3). The average thickness of the foil used in the experiments was 15.6±1.1 μm. XPS analyses for consecutive 180 nm deep sputtering intervals on Al foil after 60 h of reaction at 500 °C and atmospheric pressure are presented in Fig. 10.

The binding energy for the Al 2p electrons near the surface lies at approximately 74 eV. Deeper into the material, we can observe a shift for some of the electrons towards 72 eV. These binding energies are related to the electronic structures of oxide or hydroxide materials in the Al^{3+} state and pure elemental Al, respectively [38,39]. This shows that there is a mixed state containing pure Al and Al in its oxidized state in the region just below the surface. Simultaneously, a corresponding decreasing trend in intensity can be seen for O 1s electrons. Oxygen atoms with a binding energy of 531 eV are assigned to the alumina matrix. Subtle variations in binding energy can indicate the presence of, e.g., strongly adsorbed oxygen, OH–, or H_2O, with a binding energy towards 532.3 eV, or oxygen species such as AlO(OH), with a lower binding energy at 530.2 eV [40]. Looking at the obtained O 1s signal in Fig. 10, the peak maximum is located at 531 eV, which is indicative of Al_2O_3. However, the presence of O 1s electrons with binding energies at 530.2 (AlOOH) and 532.3 eV (adsorbed H_2O) can result in a convoluted signal similar to the measured signal. This means that the XPS results do not completely confirm the presence of Al_2O_3. Confirmation was given by grazing incidence reflectance FT-IR measurements (Fig. 11). The main absorption band has a maximum near 950 cm^{-1}, indicating Al–O vibrations in amorphous Al_2O_3, with a shoulder near 700 cm^{-1}. For the untreated material, the band at 950 cm^{-1} is indicative of the thin passivation Al_2O_3 layer [41,42]. The increased absorbance after the reaction with superheated steam indicates the growth of amorphous Al_2O_3 and effective penetration of the superheated steam beyond the passivation layer. The shoulder near 700 cm^{-1} can be assigned to asymmetric Al–O stretching in the AlO_4 tetrahedra. The second band near 555 cm^{-1} is in the range of bending and symmetric stretching of Al–O in AlO_6 octahedra, although these are more often seen as broad bands [43]. Additionally, a weak and broad absorption band is observed between approximately 3000 and 3600 cm^{-1}. This band pattern can be assigned to the stretching vibrations of surface hydroxyl groups. The increasing absorbance at approximately 950 cm^{-1} indicates the growth of amorphous Al_2O_3 after reaction with superheated steam. This shows that the passivation layer can be penetrated by superheated steam under moderate reaction conditions and that aluminium can be activated towards further oxidation.

Based on XPS and grazing incidence FT-IR, species near the surface are either metallic aluminium or amorphous Al_2O_3. Based on the atomic ratios between Al and O determined by XPS, the degree of oxidation from Al into Al_2O_3 was approximated in Fig. 12 for the different sputtering steps, which exhibited a downwards linear trend in the degree of oxidation between Al and Al_2O_3 below the surface of the Al foil. Extrapolation of the linear trend projects that partial oxidation of aluminium is possible up to 2.1 μm below the surface for reactions at atmospheric pressures; taking the dimensions of the material into account, this represents a clear improvement over the use of Al–10Si.

3.4. *Effect of reaction conditions on continuing oxidation*

Chemical and morphological changes were observed at 500 °C and atmospheric pressure, but the generation of H_2 remained below the detection limit. Reaching higher yields requires improved interaction between steam and fuel and deeper penetration of the steam. Varying the temperature and pressure of the system influences the steam characteristics for better interaction with aluminium. In the desired reaction range, the steam viscosity and steam enthalpy are the main parameters that are linearly correlated with temperature. These parameters vary less with pressure. However, the density of the steam is largely influenced by pressure and less influenced by temperature [44]. In the reactor setup, the incoming water flow was set at 2.5 g/min, and the reactor volume was fixed. A higher density of steam at higher pressures corresponds to a lower flow rate and longer interaction time inside the reactor. Reactions at high temperatures and increased pressures result in longer interactions between high-enthalpy steam and the aluminium material. This affects the adsorption of atoms onto the surface and penetration into the core of the material. Other characteristics of water under the studied reaction conditions, such as ionic products or heat capacity, can also influence the oxidation reaction [45].

Experiments at different temperatures (450, 500 and 550 °C) and different pressures (1, 5 and 10 barG) were evaluated in terms of the degree of aluminium conversion and morphological or chemical changes. All the oxidation reactions lasted for 6 h. The degree of conversion was calculated based on the theoretically possible volume of H_2 generated for the full oxidation of Al into Al_2O_3 for the high-temperature steam oxidation reaction (1245 mL H_2/g_{Al}). H_2 can be detected starting at 450 °C at pressures of 1 barG and higher when Al foil is used. EDS mapping of the surface of the reacted foil and generated H_2 revealed a consistent trend between oxidation near the surface by the ratio of O to Al (Fig. 13, left) and the degree of conversion (Fig. 13, right). Both temperature and pressure positively affect both parameters, with the conversion reaching approximately 2 % for the reactions at 550 °C and 10 barG.

The effects of the reaction temperature on the surface morphology before and after high-temperature steam oxidation at 10 barG are shown in Fig. 14. Low beam energies of 2 keV result in observations of changes

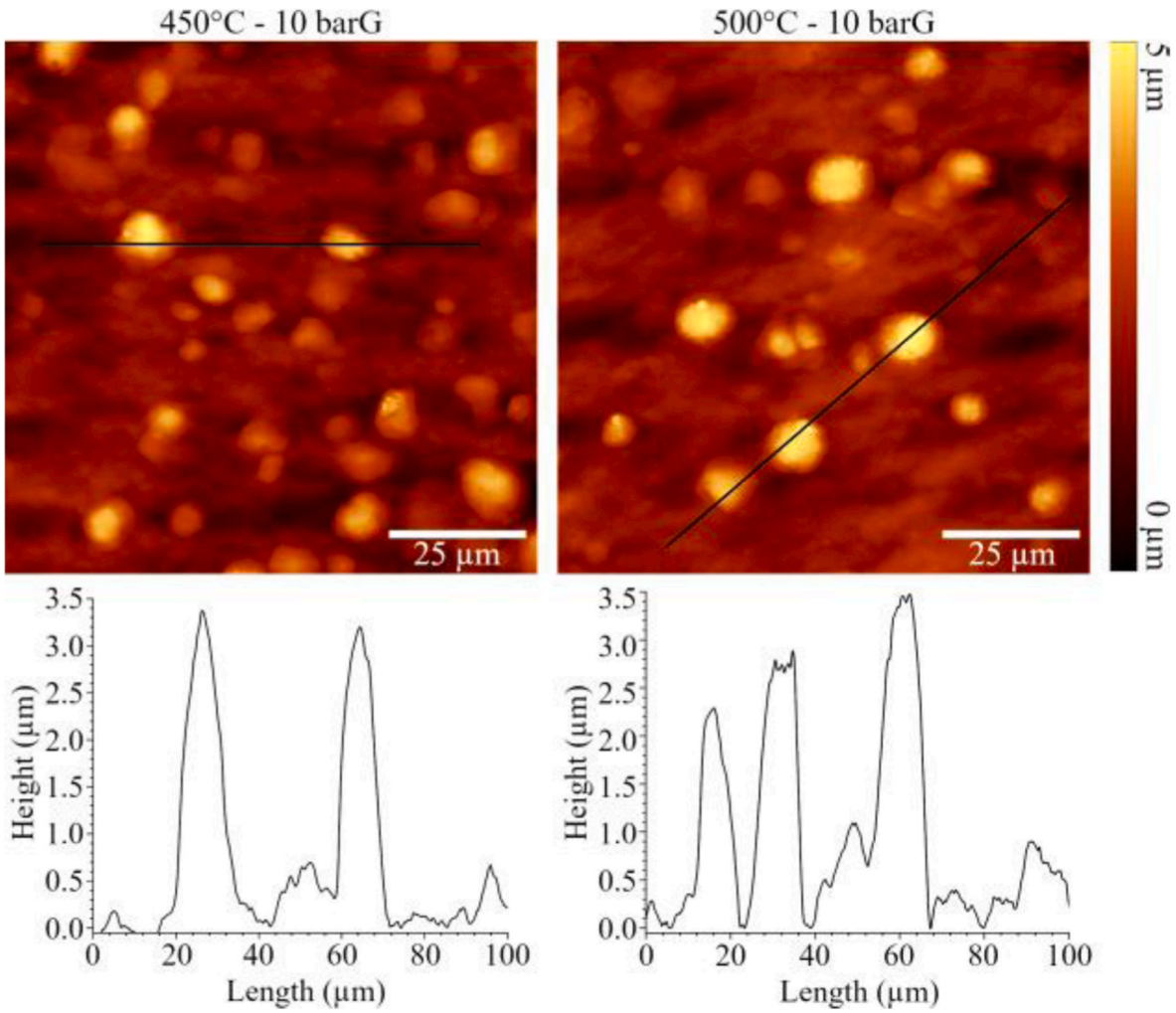

Fig. 16. AFM analysis of larger features observed after reaction with superheated steam for 6 h at 450 °C and 10 barG and at 500 °C and 10 barG. Measurement details: AC tapping mode, 100 × 100 µm^2, 1 s scan speed, 512 × 512 data points.

close to the surface. In the top row, at low magnification, spherical features appear at the surface for all the evaluated temperatures. At higher magnifications, only local changes are observable after the oxidation reaction at 450 °C and 10 barG. The interstitial space between these features appears mostly unchanged. At higher temperatures of 500 and 550 °C, the microstructure in the interstitial space clearly changes as well. The micrographs in the second and third rows, taken at higher magnifications, show microcracks and larger cracks appearing at temperatures of 500 °C and 550 °C, respectively. Oxidation at higher temperatures seems to cover the entire surface and results in a more severe alteration of the microstructure. The presence and evolution of microcracks are important for the oxidation of aluminium. Owing to its lower free Gibbs energy, water in its liquid form is a stronger oxidizer than water in its vaporized form, which should result in an easier oxidation yield of aluminium. However, this is not the case, as the presence of the passivation layer inhibits the interaction between aluminium and water in its liquid form. Harsher activation conditions or different methods are needed when oxidizing with water in its liquid form. However, this passivation layer can be penetrated by steam. The initial oxidation of aluminium due to penetrating steam creates mechanical stresses in the material and causes microcracks to form near the surface. Further interaction between steam and aluminium becomes easier and oxidizes faster. Although steam is a weaker oxidizing agent than liquid water is, the oxidation of aluminium with steam allows for more gentle activation conditions than oxidation with liquid water does [27,46].

For reactions at 450 °C and 10 barG, surface EDS analysis (Fig. 15) revealed an increasing degree of oxidation over the whole surface compared with that of the untreated foil. In addition, it appears that the spherical features have a relatively greater degree of oxidation than the space between the spheres does. Diffusion of the alloy elements, i.e., Fe, is not clearly observed in the interstitial area. The iron content seems to increase slightly around the spherical features. An increasing trend in the degree of oxidation can be seen for the reaction at 500 °C and 10 barG, again with a higher degree of oxidation for the spherical artefacts. The diffusion of iron to the surface, as well as in the interstitial area, seems to increase. Overall, it seems that oxidation at elevated pressures results in stress-induced changes in morphology. First, these changes are observed as spherical lumps, which eventually result in the formation of cracks and microcracks. These factors can possibly influence any further interaction between steam and aluminium.

If we analyse the spherical lumps with AFM, it becomes apparent that they extend distinctly above the surface of the foil. AFM scans for reactions at 10 barG and 450 or 500 °C (Fig. 16) show that these measurements are up to 3.5 µm high, which is substantial compared with the foil thickness of approximately 16 µm. AFM scans after reactions at 550 °C and 10 barG were not possible due to measurement limitations. This observation suggests the appearance of even larger features on the surface.

Optical profilometry (Fig. 17) allows us to obtain a good representation of more irregular surface morphologies on a larger scale for comparison with those of untreated Al-Foil. The surface morphologies are different after reactions at 10 barG and temperatures of 450 °C,

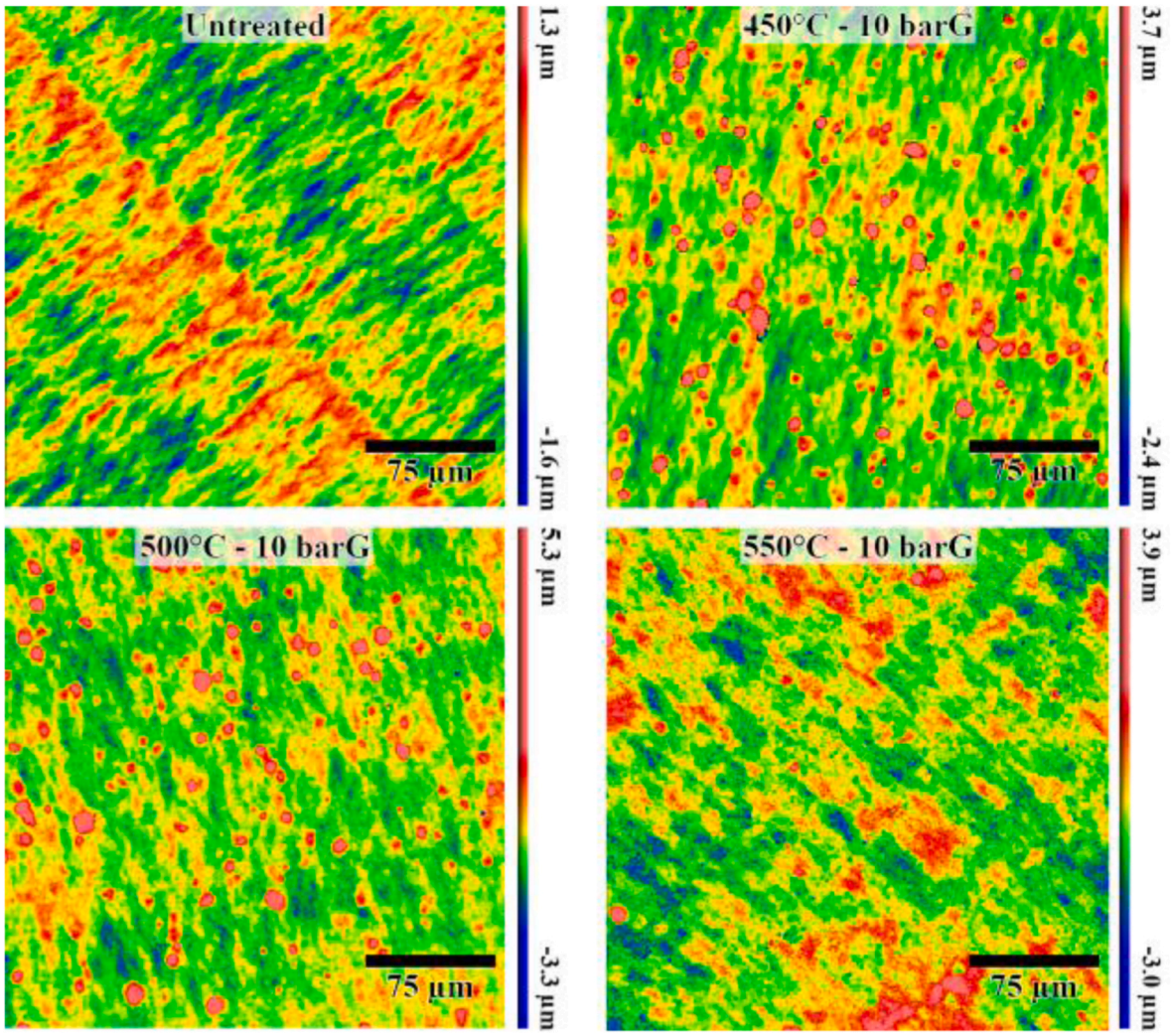

Fig. 17. Surface morphology by optical profilometry for untreated aluminium and for aluminium after reactions at 10 barG and temperatures of 450 °C, 500 °C or 550 °C (6 h) Scan details: 300 × 300 µm^2; The colour scale representation from green to red is set by the 3σ variation interval of all measured data points; Objective: 50× with FOV 167 × 167 µm. (For interpretation of the references to colour in this figure legend, the reader is referred to the Web version of this article.)

500 °C or 550 °C. The spherical features are well defined for the 2 reactions at 450 °C and 500 °C and appear to grow scattered over largely unaltered surfaces. At 550 °C, these features appear to be masked under a more irregular, and possibly more oxidized, surface. Oxidation tends to cover a larger part of the surface and becomes less local with increasing temperature.

When the pressure towards the onset of the oxidation reaction is evaluated, spherical features are already formed at reactor pressures lower than 10 barG. However, at reactor pressures of 1 and 5 barG and temperatures of 500 °C, microcracks or larger cracks in the interstitial space are not visible (Fig. 18). Microcracks only seem to appear at pressures of 10 barG; it is expected that these cracks serve as diffusion channels and enhance the interaction between penetrating superheated steam and fresh, nonpassivated aluminium. It seems that temperatures above 500 °C and reactor pressures of 10 barG or higher are needed to achieve continued, less localized oxidation.

Like for Al-Foil, the appearance of microcracks after the reaction at 500 °C and 10 barG can also be observed for most of the granulated materials (Fig. 19). For Al-Foil, we can observe numerous microcracks after the reaction. For the granulated materials, large microcracks are, in decreasing order, present for Al-Rounded0.6, Al-Krampe, Al–10Si, Al-CutWire0.6 and Al-Spajic. They are less prominent for Al-Deco and especially Al-Merck, where neither microcracks nor larger cracks are seen as signs of oxidation onset. Based on the experiments performed to determine the onset of the oxidation reaction, there is no clear relationship between the composition or shape of the aluminium material and the appearance of cracks and microcracks during the reaction. However, the appearance of cracks correlates with the change in the ratio of oxygen to aluminium at the surface of the material before and after the reaction, as determined by EDS (Figs. 5 and 20). Al-Deco and Al-Merck, with negligible numbers of cracks, have by far the lowest degree of oxidation near the surface. The O/Al ratio increased from 0.016 to 0.060 after the reaction for Al-Merck. With respect to the granulated material resulting in many cracks, the Al-Rounded material has the highest O/Al ratio, which increases from 0.073 to 0.535 after the reaction. For this sample, large microcracks can be observed spread out over the surface. These findings again confirm that the degree of oxidation at the surface coincides with morphological changes that can further influence the interaction between steam and aluminium.

Pressure-induced cracks are expected to form additional pathways for the steam to interact with fresh aluminium and help oxidize a larger fraction of the aluminium. However, the current reaction conditions for granulated matter do not generate detectable amounts of H_2 during oxidation. H_2 generation was detected when Al-Foil was used as the source material. The appearance of larger microcracks for some of the granulate matter does not compensate for the lower active surface area of the granulates. Theoretically, 1245 mL H_2 per g_{Al} can be generated for the full conversion of Al into Al_2O_3 via the superheated steam oxidation

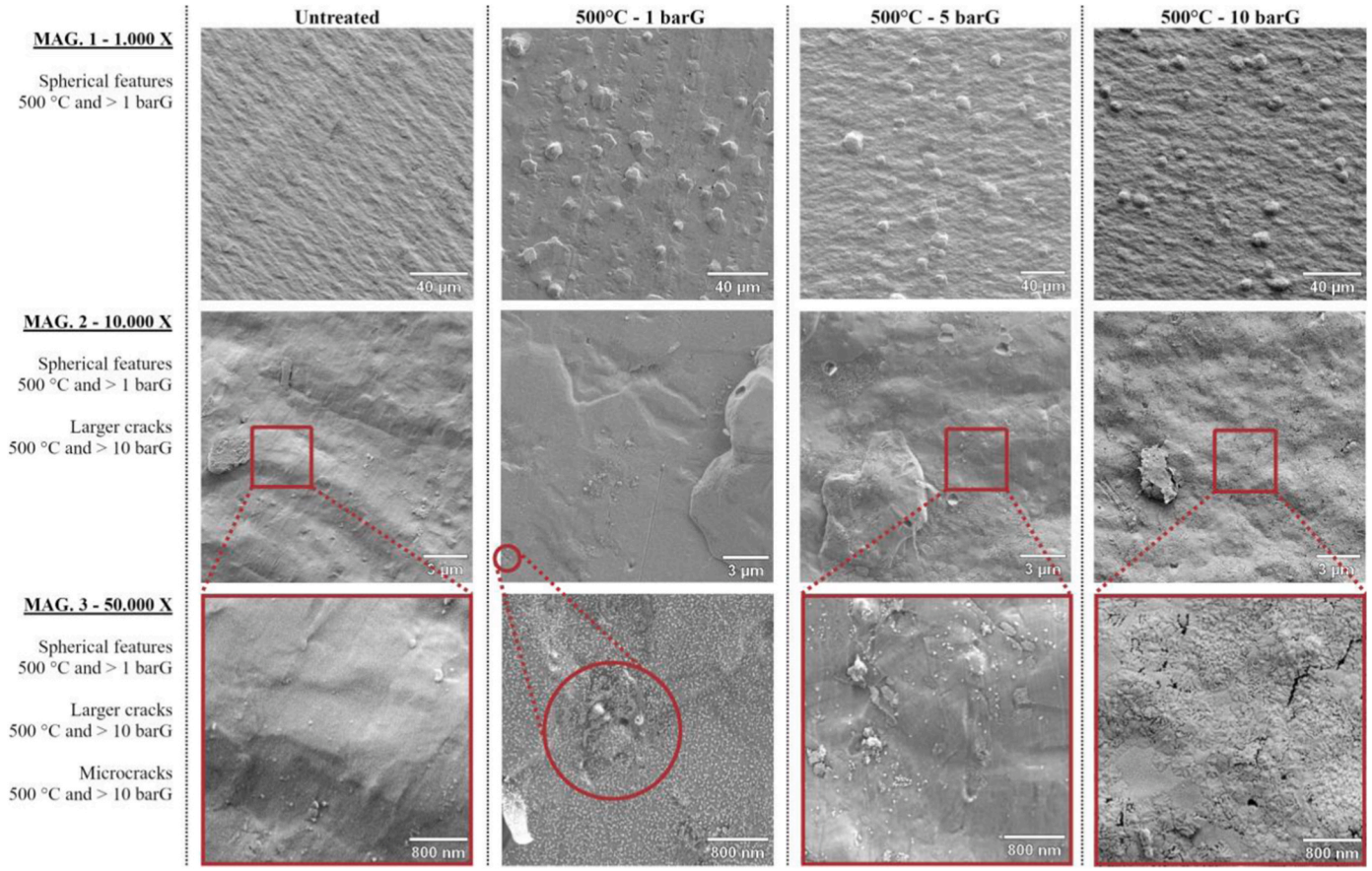

Fig. 18. SEM images of the Al-Foil surface after reaction at 500 °C (6 h) for reactor pressures of 1, 5 and 10 barG and comparison with those of the untreated Al-Foil surface (ETD detector, accelerating voltage: 2 kV). Magnifications: Top row: 1.000×, Middle row: 10.000X, Bottom row: 50.000X

reaction. The generation of H_2 for all the evaluated reactions when Al-Foil is used as the source material is shown in Fig. 21. The generation was limited to approximately 2 % after reacting for 6 h at 550 °C and 10 barG. The trends observed in the generated H_2 correlate with previous observations of the surface morphology of aluminium after the reaction.

Superheated steam at 10 barG and temperatures above 500 °C creates new pathways for deeper penetration of the steam into the aluminium core. The improved interaction in combination with the large surface area and low thickness of the aluminium foil results in oxidation beyond the passivation layer and increased generation of H_2. The results of the present study demonstrate that the interaction between superheated steam and aluminium results in detectable oxidation under the investigated conditions for all the examined fuels. The results indicate pronounced differences in reactivity among the various fuels, with fuel composition, shape and dimensions, and reaction conditions influencing the visible outcome. For aluminium foil, H_2 was detected as a physical confirmation of the proposed oxidation reaction. Chemical and morphological changes confirmed the reactivity of the other fuels. Limitations in the presented work for the superheated steam activation of safe-to-transport aluminium materials are found in the low penetration depth of steam relative to the size of the Al materials under the examined reaction conditions. This relative penetration depth—which is greatest for the foil—is directly related to the conversion of aluminium and the generation of H_2. The migration of elements occurs from the start of the reaction, which is known to influence the final reactivity. However, this work does show that changes in the microstructure are seen and are different for various fuels. This observation highlights the potential to further enhance fuel reactivity through deliberate optimization of both reaction parameters and fuel design.

4. Conclusions

Dry steam-assisted oxidation was studied for several aluminium materials of different shapes and compositions in a laboratory-scale batch reactor. The exposure of fuels to superheated steam at increased pressure creates additional pathways to overcome the passivation layer. The continued diffusion of O atoms towards a clean aluminium surface results in their transformation into an oxide material, which is confirmed by the detection of H_2. Pathways created for easier migration of atoms and ions towards the free active surface can be connected to morphological changes in the material. Granule shape and size, composition, grain orientation, and the presence of defects can influence the onset of the reaction and the creation of pathways for interaction with steam.

The use of superheated steam at atmospheric pressure results in the initial onset of the oxidation reaction via local chemical and morphological changes near the surface. However, the use of pressurized superheated steam is required to continue oxidation and confirm the reactivity via the detection of H_2. Continued oxidation seems to require the growth of microcracks, which appear after interaction with superheated steam at temperatures above 500 °C and pressures above 10 barG. These conditions allow breaking through the passivation layer, which spontaneously forms a protective barrier on the surface of aluminium.

The active surface area seems to be crucial for obtaining a sufficient yield to confirm the oxidation of the aluminium surface via H_2 detection. During this study of the initial phases of oxidation, composition seemed to be a less decisive factor. The diffusion of alloying elements or impurities in the aluminium might influence further oxidation, as local changes in composition near the surface were already present during

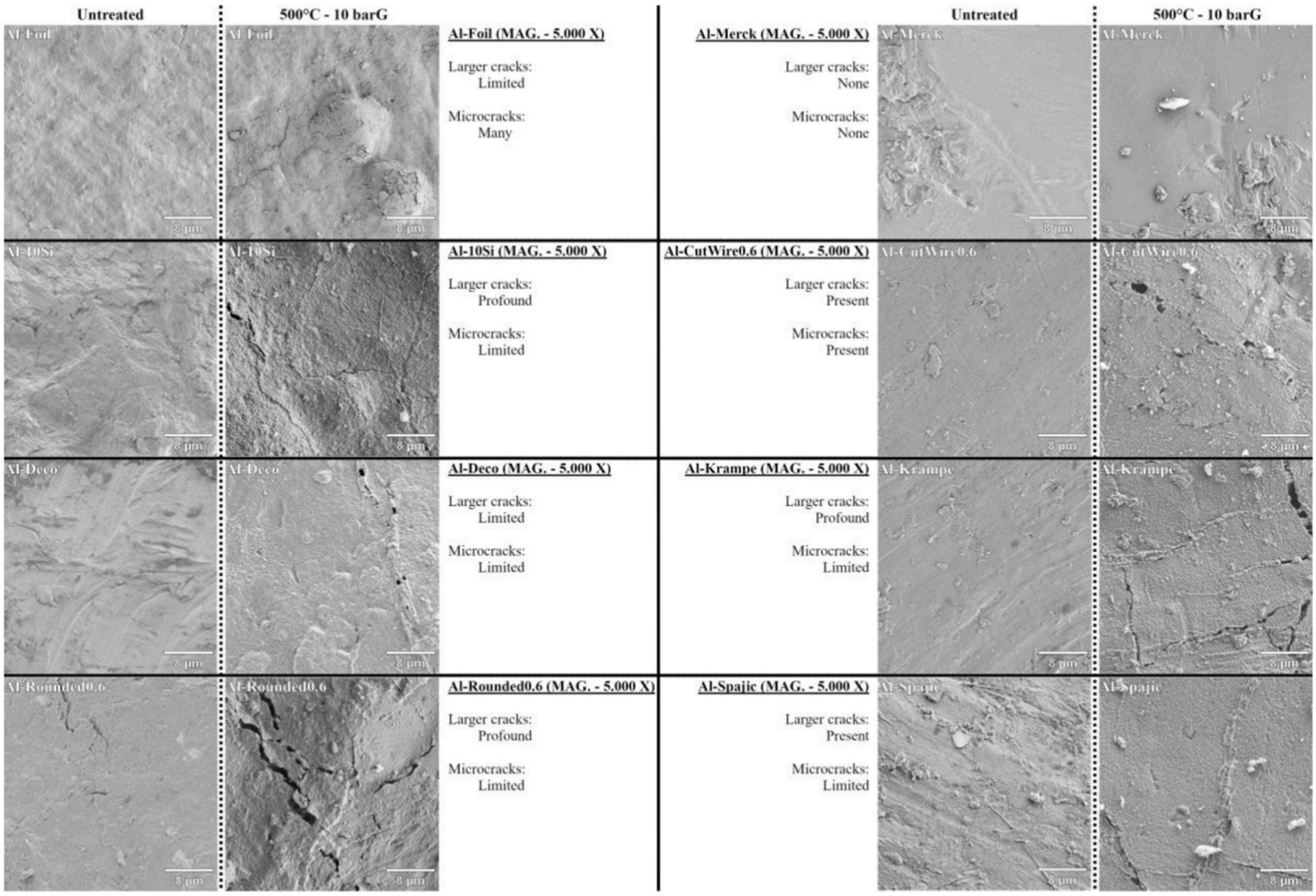

Fig. 19. SEM analysis of microcracks on the surfaces of different aluminium granulates before and after 6 h of oxidation (ETD detector, accelerating voltage: 2 kV). Magnification: 5.000×.

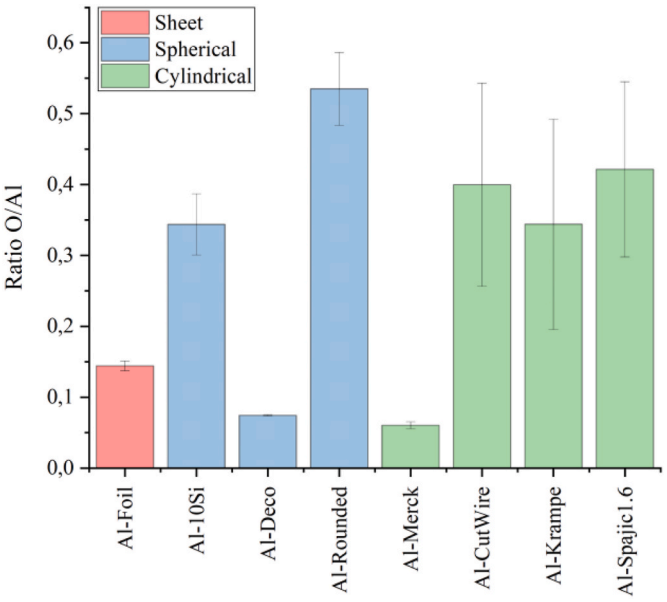

Fig. 20. O-to-Al ratio from EDS analysis performed on the surfaces of different Al materials after reaction with superheated steam at 500 °C and 10 barG for 6 h, with y-error bars related to variations between individual measurement sites. EDS analysis area magnification: 5.000×.

this initial stage of oxidation.

The presented research reveals possibilities for oxidizing larger particulate matter within a dry oxidizing environment and potentially extracting heat and producing hydrogen for energy supply.

CRediT authorship contribution statement

N.W. Van de Velde: Writing – review & editing, Writing – original draft, Visualization, Validation, Methodology, Investigation, Formal analysis, Data curation. **A. Drinčić:** Validation, Methodology, Investigation. **M. Grom:** Resources, Investigation, Conceptualization. **B. Likozar:** Writing – review & editing, Resources. **B. Genorio:** Writing – review & editing, Investigation. **M. Haller:** Writing – review & editing, Resources, Project administration, Funding acquisition, Conceptualization. **I. Jerman:** Writing – review & editing, Writing – original draft, Supervision, Resources, Project administration, Methodology, Investigation, Funding acquisition, Conceptualization.

Funding

The presented work contributes to the REVEAL research project supported by the European Commission under the Horizon Europe programme for Research and Innovation (call HORIZON-CL5-2021-D2-01). Co-funded by the European Union under Grant Agreement No. 101069492 and the State Secretariat for Education, Research, and Innovation (SERI). The views and opinions expressed are those of the author(s) only and do not necessarily reflect those of the European Union or CINEA. Neither the European Union nor the granting authority

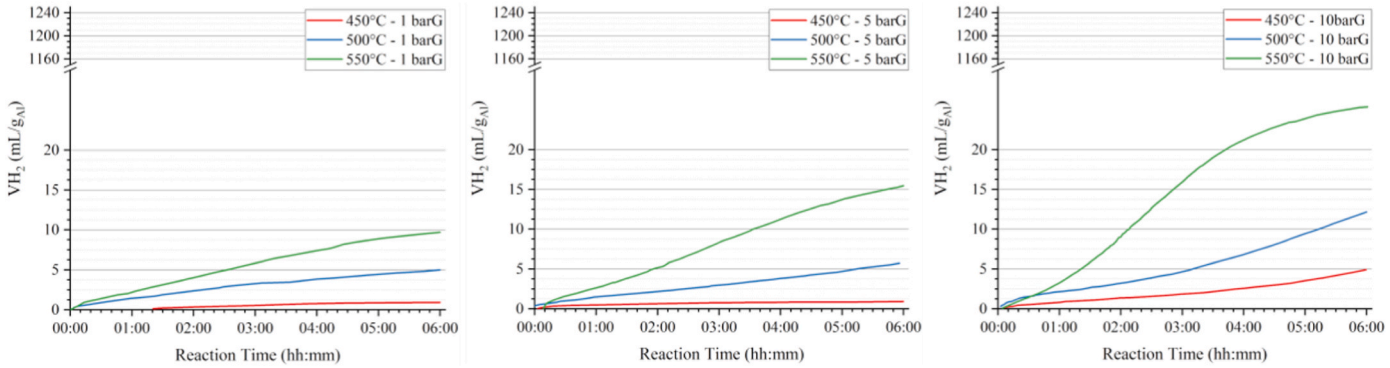

Fig. 21. Generated volumes of H_2 after the oxidation of Al-Foil with superheated steam for 6 h at 450 °C, 500 °C, and 550 °C. Left: Experiments at 1 barG, Middle: Experiments at 5 barG, Right: Experiments at 10 barG

can be held responsible for them.

Declaration of competing interest

The authors declare that they have no known competing financial interests or personal relationships that could have appeared to influence the work reported in this paper.

References

[1] International Energy Agency. Managing seasonal and interannual variability of renewables. 2023.

[2] International Energy Agency. Credible pathways to 1.5 °C - four pillars for action in the 2020s. 2023.

[3] Hossain E, Faruque H, Sunny Md, Mohammad N, Nawar N. A comprehensive review on energy storage systems: types, comparison, current scenario, applications, barriers, and potential solutions, policies, and future prospects. Energies 2020;13:3651. https://doi.org/10.3390/en13143651.

[4] Olabi AG, Onumaegbu C, Wilberforce T, Ramadan M, Abdelkareem MA, Al – Alami AH. Critical review of energy storage systems. Energy 2021;214:118987. https://doi.org/10.1016/J.ENERGY.2020.118987.

[5] Mitali J, Dhinakaran S, Mohamad AA. Energy storage systems: a review. Energy Storage Sav 2022;1:166–216. https://doi.org/10.1016/J.ENSS.2022.07.002.

[6] Elalfy DA, Gouda E, Kotb MF, Bureš V, Sedhom BE. Comprehensive review of energy storage systems technologies, objectives, challenges, and future trends. Energy Strategy Rev 2024;54:101482. https://doi.org/10.1016/j.esr.2024.101482.

[7] Hannan MA, Wali SB, Ker PJ, Rahman MSA, Mansor M, Ramachandaramurthy VK, et al. Battery energy-storage system: a review of technologies, optimization objectives, constraints, approaches, and outstanding issues. J Energy Storage 2021;42:103023. https://doi.org/10.1016/j.est.2021.103023.

[8] Baeuerle YI, Arpagaus C, Haller MY. A review of seasonal energy storage for net-zero industrial heat: thermal and Power-to-X storage including the novel concept of renewable metal energy carriers. Energies 2025;18:2204. https://doi.org/10.3390/en18092204.

[9] Guerra OJ, Dalvi S, Thatte A, Cowiestoll B, Jorgenson J, Hodge B-M. Towards robust and scalable dispatch modeling of long-duration energy storage. Renew Sustain Energy Rev 2025;207:114940. https://doi.org/10.1016/j.rser.2024.114940.

[10] Borri E, Tafone A, Romagnoli A, Comodi G. A review on liquid air energy storage: history, state of the art and recent developments. Renew Sustain Energy Rev 2021;137:110572. https://doi.org/10.1016/j.rser.2020.110572.

[11] Das LM. On-board hydrogen storage systems for automotive application. Int J Hydrog Energy 1996;21:789–800. https://doi.org/10.1016/0360-3199(96)00006-7.

[12] Miranda T, Montero I, Sepúlveda FJ, Arranz JI, Rojas CV, Nogales S. A review of pellets from different sources. Materials 2015;8:1413–27. https://doi.org/10.3390/ma8041413.

[13] Li Xueqin, Chen Zhuo, Liu Peng, Wang Zhiwei, Sun Tanglei, Wu Shiyong, et al. Oriented pyrolysis of biomass for hydrogen-rich gas and biochar production: an energy, environment, and economic assessment based on life cycle assessment method. Int J Hydrog Energy 2024;62:979–93. https://doi.org/10.1016/j.ijhydene.2024.03.160.

[14] Bergthorson JM. Recyclable metal fuels for clean and compact zero-carbon power. Prog Energy Combust Sci 2018;68:169–96. https://doi.org/10.1016/j.pecs.2018.05.001.

[15] Shkolnikov EI, Zhuk AZ, Vlaskin MS. Aluminum as energy carrier: feasibility analysis and current technologies overview. Renew Sustain Energy Rev 2011;15:4611–23. https://doi.org/10.1016/j.rser.2011.07.091.

[16] Trowell KA, Goroshin S, Frost DL, Bergthorson JM. Aluminum and its role as a recyclable, sustainable carrier of renewable energy. Appl Energy 2020;275. https://doi.org/10.1016/j.apenergy.2020.115112.

[17] Padamata SK, Singh K, Haarberg GM, Saevarsdottir G. Review—primary production of aluminium with oxygen evolving anodes. J Electrochem Soc 2023;170:073501. https://doi.org/10.1149/1945-7111/ace332.

[18] Haller MY, Carbonell D, Dudita M, Zenhäusern D, Häberle A. Seasonal energy storage in aluminium for 100 percent solar heat and electricity supply. Energy Convers Manag X 2020;5:100017. https://doi.org/10.1016/J.ECMX.2019.100017.

[19] Bergthorson JM, Goroshin S, Soo MJ, Julien P, Palecka J, Frost DL, et al. Direct combustion of recyclable metal fuels for zero-carbon heat and power. Appl Energy 2015;160:368–82. https://doi.org/10.1016/J.APENERGY.2015.09.037.

[20] Meroueh L, Eagar TW, Hart DP. Effects of Mg and Si Doping on Hydrogen Generation via Reduction of Aluminum Alloys in Water. ACS Appl Energy Mater 2020;3:1860–8. https://doi.org/10.1021/acsaem.9b02300.

[21] Manilevich FD, Pirskyy YuK, Kutsyi AV, Berezovets VV, Yartys VA. Aluminium as an efficient energy storage substance for the catalysed generation of hydrogen from water. J Energy Storage 2024;96:112748. https://doi.org/10.1016/j.est.2024.112748.

[22] Barelli L, Trombetti L, Zhang S, Ersoy H, Baumann M, Passerini S. Potential of aluminum as a metal fuel for supporting EU long-term energy storage needs. Adv Mater Technol 2024;9:2302206. https://doi.org/10.1002/admt.202302206.

[23] Etminanbakhsh M, Reza Allahkaram S. Reaction of aluminum particles with superheated steam to generate hydrogen gas as a readily useable clean fuel. Fuel 2023;332:126011. https://doi.org/10.1016/j.fuel.2022.126011.

[24] Yavor Y, Goroshin S, Bergthorson JM, Frost DL, Stowe R, Ringuette S. Enhanced hydrogen generation from aluminum-water reactions. Int J Hydrog Energy 2013;38:14992–5002. https://doi.org/10.1016/j.ijhydene.2013.09.070.

[25] Agote-Arán M, Welte B, Freeman R, Mutti N, Haller M, Heel A. Al6060 cut wire granules for Al-water reaction: evaluation of reaction conditions and granule treatments. Int J Hydrog Energy 2025;117:430–41. https://doi.org/10.1016/j.ijhydene.2025.03.117.

[26] Gao X, Wang C, Hou Y, Zhao L, Bai W, Che D. Experimental study on characteristics and mechanism of hydrogen production from aluminium–water reaction for carbon-free power generation. Fuel 2025;380:133206. https://doi.org/10.1016/j.fuel.2024.133206.

[27] Trowell KA, Goroshin S, Frost DL, Bergthorson JM. The use of supercritical water for the catalyst-free oxidation of coarse aluminum for hydrogen production. Sustain Energy Fuels 2020;4:5628–35. https://doi.org/10.1039/d0se00996b.

[28] Chase MW. NIST-JANAF thermochemical tables. fourth ed. American Institute of Physics; 1998.

[29] Nguyen HQ, Shabani B. Proton exchange membrane fuel cells heat recovery opportunities for combined heating/cooling and power applications. Energy Convers Manag 2020;204:112328. https://doi.org/10.1016/j.enconman.2019.112328.

[30] Haller MY, Amstad D, Dudita M, Englert A, Häberle A. Combined heat and power production based on renewable aluminium-water reaction. Renew Energy 2021;174:879–93. https://doi.org/10.1016/j.renene.2021.04.104.

[31] Teichert M, Haller MY, Sick F. Aluminium redox cycle in comparison to pressurized hydrogen for the energy supply of multi-family houses. Appl Energy Combust Sci 2023;13:100098. https://doi.org/10.1016/J.JAECS.2022.100098.

[32] Boudreau P, Johnson M, Bergthorson J M. Techno-economic assessment of aluminum as a clean energy carrier to decarbonize remote industries. Energy Adv 2024;3:1919–31. https://doi.org/10.1039/D4YA00151F.

[33] Huang Y, Risha GA, Yang V, Yetter RA. Combustion of bimodal nano/micron-sized aluminum particle dust in air. Proc Combust Inst 2007;31:2001–9. https://doi.org/10.1016/j.proci.2006.08.103.

[34] International alloy designations and chemical composition limits for wrought aluminum and wrought aluminum alloys The Aluminum. Association 2018;23:1–34.

[35] Davis JR. Aluminum and aluminum alloys. Alloy Underst Basics 2001. Page range 351-416.

[36] Over H, Seitsonen AP. Oxidation of metal surfaces. Science 2002;297:2003–5. https://doi.org/10.1126/science.1077063.

[37] Nylund A, Mizuno K, Olefjord I. Influence of Mg and Si on the Oxidation of Aluminum. Oxid Met 1998;50:309–25. https://doi.org/10.1023/A:1018844506192.
[38] Beccat P, Silva PD, Huiban Y, Kasztelan S. Quantitative surface analysis by xps (X-Ray photoelectron spectroscopy): application to hydrotreating catalysts. Oil Gas Sci Technol 1999;54:487–96. https://doi.org/10.2516/ogst:1999042.
[39] Sherwood PMA. Introduction to studies of aluminum and its compounds by XPS. Surf Sci Spectra 1998;5:1–3. https://doi.org/10.1116/1.1247880.
[40] Peng J, Sun Q, Zhai Z, Yuan J, Huang X, Jin Z, et al. Low temperature, solution-processed alumina for organic solar cells. Nanotechnology 2013;24:484010. https://doi.org/10.1088/0957-4484/24/48/484010.
[41] Ludwig B, Burke TT. Infrared spectroscopy studies of aluminum oxide and metallic aluminum powders, part I: thermal dehydration and decomposition. Powders 2022;1:47–61. https://doi.org/10.3390/powders1010005.
[42] Kaltchev M, Tysoe WT. An infrared spectroscopic investigation of thin alumina films: measurement of acid sites and surface reactivity. Surf Sci 1999;430:29–36. https://doi.org/10.1016/S0039-6028(99)00376-3.
[43] Busca G. The surface of transitional aluminas: a critical review. Catal Today 2014;226:2–13. https://doi.org/10.1016/j.cattod.2013.08.003.
[44] TLV. TLV superheated steam table. 2025.
[45] Yakaboylu O, Harinck J, Smit KG, De Jong W. Supercritical water gasification of biomass: a literature and technology overview. Energies 2015;8:859–94. https://doi.org/10.3390/en8020859.
[46] Vlaskin MS, Valyano GE, Zhuk AZ, Shkolnikov EI. Oxidation of coarse aluminum in pressured water steam for energy applications. Int J Energy Res 2020;44:8689–715. https://doi.org/10.1002/er.5561.